IEEE Access
Multidisciplinary ⋮ Rapid Review ⋮ Open Access Journal

Received 23 May 2022, accepted 18 June 2022, date of publication 24 June 2022, date of current version 1 July 2022.

Digital Object Identifier 10.1109/ACCESS.2022.3185996

Project and Performance Evaluation on an Optimized 18-Pulse Rectifier With Delta-Differential Connection ATRU and Cascaded Boost Converters for More Electric Aircraft

ANA L. SOARES, ANTÔNIO C. O. NETO, VITOR F. BARBOSA, GUSTAVO B. LIMA, AND LUIZ C. G. FREITAS

Faculty of Electrical Engineering, Federal University of Uberlândia, Uberlândia, MG 38400-902, Brazil

Corresponding author: Luiz C. G. Freitas (lcgfreitas@ufu.br)

This work was supported in part by National Council for Scientific and Technological Development (CNPq) under Grants 140541/2020-9, 303350/2019-9, 304479/2017-9, 304489/2017-4; in part by Minas Gerais Research Funding Foundation (Fapemig), in part by Coordination for the Improvement of Higher Education Personnel (CAPES), and in part by Federal University of Uberlandia (Process 23117.043835/2022-66).

ABSTRACT This paper presents the design and analysis of a special Rectifier Unit (RU) composed of a Delta-Differential Symmetric 18-pulse Autotransformer and cascade Boost converters for applications in More Electric Aircraft (MEA), which is denominated as RU-DDS18PATR+Boost. The cascaded Boost converters provide dc-link regulation, while eliminating the need to use interphase transformers (IPTs), interphase rectors (IPRs), and zero-sequence blocking transformers (ZSBTs), thus contributing toward decreasing the complexity and at the same time increasing reliability. The proposed RU-DDS18PATR+Boost operates with an active current shaping strategy in order to meet the harmonic content restrictions imposed by the DO-160F standard, while allowing for the design of a DDS18PATR with a notable kVA rating of 21.03%. The performance of the RU-DDS18PATR+Boost was analyzed operating in a system with a supply voltage of 115VAC and variable frequency in the range of 360Hz to 800Hz, which is converted to 540VDC. Experimental results are presented corroborating the theory put forward herein, especially with regard to meeting the limits imposed by the DO-160F standard.

INDEX TERMS Aircraft, autotransformer, dc distribution, harmonic distortion, rectifier.

I. INTRODUCTION

With the aim of arriving at more efficient and sustainable transport, over recent decades there has been a greater electrification of both civil and military aircraft, giving rise to the concept of More Electric Aircraft (MEA). This has resulted in the replacement of pneumatic, mechanical and hydraulic systems with electrical systems, which in itself brings benefits in terms of environmental impact, cost savings, maintenance, noise pollution, reliability, as well as aiding in power management and increasing the efficiency of the power distribution system [1], [2].

However, this led to an increase in the demand for electrical energy on board, as well as in the complexity of the Electric Power System (EPS) in aircraft [3]. This EPS is a hybrid system that is made up of distribution systems in alternating current (AC) and direct current (DC) with different voltage levels. These are connected by static converters that must comply with the MIL-STD-704 standard, and with standards that limit voltage and current total harmonic distortion (THD), such as DO-160F and ISO-1540 [4]–[6].

In terms of the AC generation and distribution used in EPSs of military and civil aircrafts, it is worth noting that, in the AC bus, voltage levels are used at 115VAC (or 230VA) with a fixed frequency equal to 400Hz, while the predominant frequency in most modern aircraft is variable, in the range of 360Hz to 800Hz. The use of AC bus with a fixed frequency (400Hz) is also seen, as found in the two best-known civil aircraft that incorporate MEA technology, the Airbus A380 and the Boeing 787, where the AC systems are converted to ±135VDC and ±270VDC, respectively [1], [3].

In order to further reduce the weight of the aircraft and, consequently, reduce fuel consumption, while improving performance, higher voltage levels on the DC power distribution

The associate editor coordinating the review of this manuscript and approving it for publication was Sudhakar Babu Thanikanti.

bus are necessary in order to reduce the weight of cables and equipment. Therefore, for future applications, the trend in the construction of civil aircraft that incorporate MEA technology has been to use DC buses with higher voltage levels (HVDC) [3], these can be a symmetrical bus at ±270VDC or single bus at 540V [8]–[12].

In this context, in [13] the authors proposed a multilevel converter consisting of four single-phase H-Bridge cells coupled to four Dual Active Bridge (DAB) DC-DC converters for each phase of the EPS. The association of several two-stage static converters (AC-DC + DC-DC) is carried out with series connection on the AC side (to constitute the current waveform with reduced THDi) and parallel connection on the DC side (to achieve the desired power at 270Vdc). Hence, the THDi achieved is excellent (3.5%), however, the chief disadvantage is the high number of semiconductors (24 static converters with 144 IGBTs), which goes on to reduce the reliability and robustness of the structure, as well as increasing switching losses and contributing to reduced efficiency. In [14], a three-phase coupled inductor-based bipolar-output active rectifier is incorporated (TCIBAR) to achieve a balanced ±270V power supply for MEA. The THDi achieved was less than 5% and the efficiency was around 95.1%. However, as also noted in [13] and in [15]–[18], the Rectifier Units (RU) are fully active and must be designed for rated power, so the structure's robustness and reliability can be compromised in designs that require higher power levels.

In light of the aforementioned, through the prioritizing of the robustness and reliability of and AC-DC convertion systems, Multipulse Rectifiers (MPR) have become more widely used [1], [7], [19]–[33]. These are powered by special transformers units which can be divided into two groups, Transformer Rectifier Unity (TRUs) and Autotransformer Rectifier Unity (ATRUs). In order to guarantee the best performance of the MPR with transformers (MPTRU) and with autotransformers (MPATRU), Interphase Transformers (IPTs) and Interphase Reactors (IPRs) are used to absorb the instantaneous voltage differences of each rectifier group.

The TRUs provide electrical isolation between the generator and the loads and process all required energy. Therefore, their weight and volume are higher when compared to ATRUs, which are not galvanically isolated. Both devices are robust, promote reduced voltage and current harmonic distortion, while ensuring high efficiency and a high power factor. However, ATRUs stand out in terms of the reduced portion of power for which they are designed. Such an operational characteristic is known as kVA rating, which is a preponderant factor in the choice of multipulse rectifiers used in MEA.

In [19], the authors proposed a 24-pulse diode rectifier which consists of a conventional four-star 12-pulse diode rectifier and an auxiliary single-phase low power full wave rectifier (ASFR - kVA rating: 3.4%) installed on the dc side. It is a robust device with reduced THDi (5.25%), however, the main transformer is designed to process all the power required by the load (kVA rating of 100%). It is also important to outline that IPTs are necessary to guarantee the desired performance. Therefore, weight and volume are the main disadvantages of this structure.

In [20], the authors presented a novel parallel configured 48-pulse rectifier with ATRU, which is made up of two 24-pulse rectifiers connected in parallel through a tapped and coupled interphase reactor. The 48-pulse ATRU kVA rating is 21.82% and the achieved THDi is 3.13%, however, there is a need to employ IPRs (kVA rating: 2.185%) and Zero-Sequence Blocking Transformers (ZSBTs) with a kVA rating of 7.57%. Furthermore, the good performance of the structure depends on the correct functioning of the IPRs and ZSBTs, which are designed to prevent zero-sequence components and ensure that the diode-bridge rectifiers (DBRs) operate independently with a 120° conduction interval on each diode. On the other hand, it should be noted that the two 24-pulse ATRU operate independently, so the damage of one unit will not result in catastrophic system failure, but only a degradation in power quality and power rating delivered to the loads.

In [21], two 20-pulse ATRUs using a 10-Phase Autotransformer are presented. Both require the use of IPTs and ZSBTs. The second differs from the first by employing a Passive Harmonic Reduction Circuit (PHRC). Excellent results were achieved (THDi less than 5% and average efficiency of 97%) and the power rating of the magnetic elements is 29.69% (without PHRC) and 30.8% (with PHRC). In [22], a 20-pulse Multiphase Staggering Autoconfigured Transformer (MSAT) is presented. This is a result of a combination of autotransformers with delta and zig-zag configuration. As also noted in [21], THDi lower than 5% and average efficiency of 97% were achieved, however, the kVA rating was around 40% of the power required by the load. In [23], the authors presented a novel 20-pulse ATRU based on a T-connected autotransformer with a kVA rating of 44.48%.

In the light of the aforementioned, one notes that many efforts are directed towards achieving remarkable improvement in power quality - low THD of voltage and current even while under variable frequency - with high efficiency and reduced weight and size. In this context, in [25], the authors analyzed 47 papers including articles, standards, books, and presented an important comparative study concerning the magnetic power ratings of different MPATRUs. In their study, these authors demonstrated that an increase in the number of pulses leads to an increase in the overall kVA rating (ATRU, IPT, ZSBT), cost, and complexity of the MPATRU, while the main power quality issues remain practically unchanged.

In this scenario, many 18-pulse ATRUs schemes prove to be a preferable option in applications involving MPATRUs [7], [24]–[31], since the power quality indicators are better than those provided by the 12-pulses ATRUs. In addition, the complexity is lower, and the efficiency is higher when compared to ATRUs of 20-pulse [23], 24-pulse [19], and 48-pulse [20] since less DBRUs are needed.

The study first presented in [28], and then confirmed in [7], [23], [25], demonstrated that the Delta-Polygon Asymmetric 18-pulse ATRU scheme is one of the best choices

TABLE 1. Comparison between the main multipulse rectifier units analyzed including the proposed RU-DDS18PATRU+Boost.

Reference / year	ATRU Scheme	ATRU kVA Rating (%)	IPTs/IPRs kVA Rating (%)	ZSBTs kVA Rating (%)	Active DC-link Voltage Control	Compliancy with DO-160F	Variable Frequency Operation (400-800Hz)	Number of Semiconductors (Switches/ Diodes)	Efficiency at Rated Load (%)	THDi (%)	Passive Filter for Power Quality Requirement	Complexity of ATRU Project
Proposed MPRU RU-DDS18PATR+Boost (2022)	Delta-Differential Symmetric	21.03	-	-	Yes	Yes	Yes	27 (3/24)	96.0	3.66	No	Low
18-pulse ATRU [7] (2020)	Delta-Polygon Asymmetric	27.5	-	-	No	Yes	Yes	18 (0/18)	98.5	6.55	Yes	Low
Interleaved DCM Buck-Boost Derived [16] (2021)	-	-	-	-	Yes	Yes	Yes	20 (8/12)	96.3	2.52	Yes	-
DCM Cuk Derived [17] (2020)	-	-	-	-	Yes	Yes	Yes	9 (3/6)	94.11	3.91	No	-
20-pulse ATRU [23] (2021)	T-connected	42.98	1.5	-	No	Yes	Yes	20 (0/20)	97.75	3.62	No	High
20-pulse ATRU [21] (2021)	T-connected	27.1	2.59	-	No	Yes	Yes	22 (0/22)	98.5	4.75	No	High
20-pulse ATRU + PHRC [21] (2021)	T-connected	27.1	-	3.7*	No	Yes	Yes	20 (0/20)	98.46	2.67	No	Medium
18-pulse ATRU [25] (2019)	Delta-Polygon Asymmetric	27.6	-	-	No	Yes	Yes	24 (6/18)	98.5	6.74	Yes	Low
18-pulse ATRU [29] (2019)	Delta-Polygon Asymmetric	31.5	-	-	No	Yes	Yes	27 (2/25)	96.9	6.7	Yes	Low

OBS: * - 3.7 (2.45 – ZSBT AND 1.25 – PHRC)

for MEA application, as it considers power quality issues, along with the fact that asymmetric schemes allow for the elimination of IPTs/IPRs and ZSBTs.

On the hand, in [32] and [33] the authors have demonstrated the huge potential of Delta-Differential Symmetric 12-Pulse and 18-Pulse ATRU for MEA application. This is because for the unitary transformation ratio, the kVA rating is significantly smaller when compared to Delta-Polygon Asymmetric 18-Pulse ATRU schemes.

Therefore, in light of the important contributions presented in [7] (published in 2020) and in [3] (published in 2021), where the authors analyzed more than two hundred (200) important papers published over the last decade, the main contribution of the article proposed herein is to present a special Rectifier Unit (RU) composed of Delta-Differential Symmetric 18-pulse ATRU (DDS-18PATRU) with cascade Boost converters, which is denominated as RU-DDS18PATR+Boost.

By filling a research gap regarding the application of the DDS-18PATRU in the MEA context, the proposed RU-DDS18PATRU+Boost is designed to operate with a specific control strategy that makes it possible to meet the harmonic content restrictions of the input currents imposed by the standard DO-160F. This is also achieved with a suitable load power share among the rectifier units, without using IPTs, IPRs, and ZSBTs nor complex ATRU schemes or complex PWM rectifiers. Additionally, it also operates with adjustable and regulated dc-link voltage. To conclude the state-of-the-art analysis, a summary of the main works analyzed is presented in Table 1. The focus is to present their main constructive characteristics and performance indicators, in comparison with the proposed RU-DDS18PATRU+Boost.

To present the results obtained and to prove the effectiveness of the proposed RU-DDS18PATRU+Boost, the remainder of this article is structured as follows, Section II outlines the system through a detailed description and a design overview of the DDS18PATRU. Section III describes the proposed control strategy and the design of the voltage and current controllers. Section IV presents the experimental results obtained in the laboratory, as well as insightful discussions. Finally, the concluding remarks are elucidated in Section V.

II. DDS-18PATRU: PRINCIPLE OF OPERATION AND DESIGN GUIDELINE

A schematic diagram of the proposed Delta-Differential Symmetric 18-pulse ATRU (DDS-18PATRU) is portrayed in Fig. 1. Three sets of voltages are produced by the DDS-18PATRU to supply three diode-bridges rectifier units (DBRUs). The dc output of each DBRU is connected as an input voltage source for a DC-DC Boost converter.

In Fig. 2, one notes the coil configuration of the DDS-18PATRU. The primary winding is connected in delta configuration across the mains supply voltages va, vb, and vc.

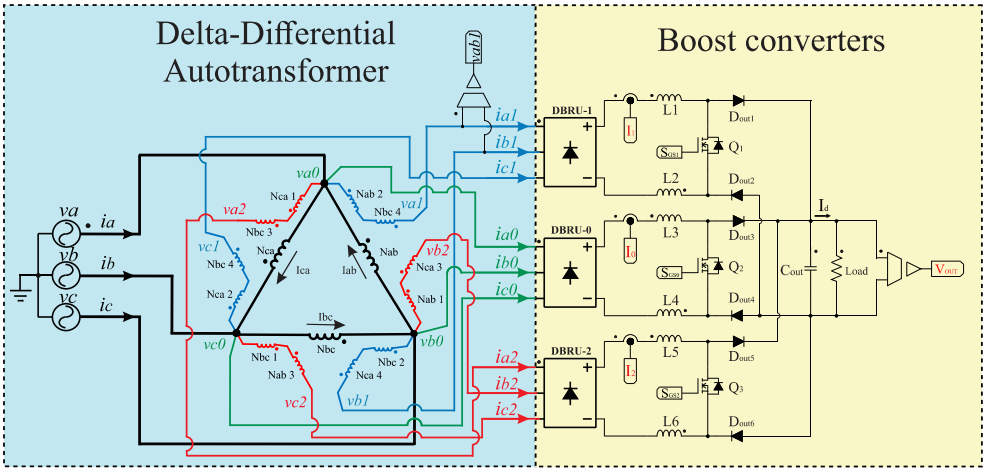

FIGURE 1. Schematic diagram of delta-differential 18-pulse ATRU and BOOST converters.

The voltages *va0, vb0* and *vc0* correspond to the secondary voltages, which are in phase with the mains supplies voltages *va, vb,* and *vc*. It allows the magnitude of secondary voltages to be the same as the original primary voltage. The auxiliary windings (marked as Nxxy being x = a, b, c; and y = 1, 2, 3, 4) are used to generate the required two voltage sets *va1, vb1, vc1,* with a phase shift equal to +20°, and *va2, vb2, vc2,* with a phase shift equal to −20°, both in relation to the secondary voltages *va0*, *vb0*, and *vc0*.

In this context, through the analysis of voltage phasor diagram depicted in Fig. 2(b), one reaches the conclusion that the phasor *Va* is equal to *Va1* + *Vab2* + *Vbc4*, and the phasor *Vaux* represents the voltage between a neutral point and the auxiliary windings. Therefore, one can conclude that the auxiliary windings are responsible for assuring the desired magnitude and phase shift of phasors *Va1* and *Va2* in relation to phasor *Va.* Analogous, phasors *Vb1, Vb2, Vc1* and *Vc2* can be obtained.

The windings representation on a three-limb core is shown in Fig. 3. Each limb has five windings, as for example, primary winding *Nab* and the auxiliary windings *Nab1*, *Nab2*, *Nab3* and *Nab4*. Those marked as *Nxx1* (being x = a, b, c) are equal to those marked as *Nxx3*, and those marked as *Nxx2* are equal to those marked as *Nxx4*.

A. DDS18PATRU: INPUT LINE CURRENT COMPOSITION

For the subsequent theoretical analysis and calculations, the following assumptions are given: 1) the leakage inductance of the DDS-18PATRU is neglected. 2) the diodes deployed in each DBRU are ideal, and 3) the average input current of each DC-DC Boost converter is equal to Io/3 (33% of the load current).

Therefore, in Fig. 3, based on the law of equal ampere-turns, one has:

$$\begin{cases} Nab \cdot iab(t) + Nab_1 \cdot iab_1(t) + Nab_4 \cdot iab_4(t) = A_{11} \\ Nbc \cdot ibc(t) + Nbc_1 \cdot ibc_1(t) + Nbc_4 \cdot ibc_4(t) = A_{12} \\ Nca \cdot ica(t) + Nca_1 \cdot ica_1(t) + Nca_4 \cdot ica_4(t) = A_{13} \end{cases} \quad (1)$$

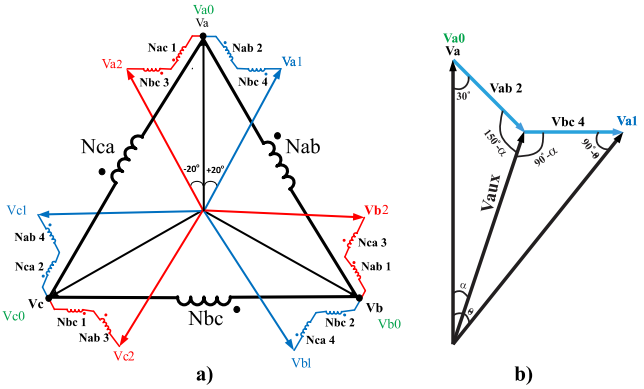

FIGURE 2. DDS-18PATRU (a) configuration scheme (b) voltage phasor diagram for phase A.

where:

$$\begin{cases} A_{11} = Nab_2 \cdot iab_2(t) + Nab_3 \cdot iab_3(t) \\ A_{12} = Nbc_2 \cdot ibc_2(t) + Nbc_3 \cdot ibc_3(t) \\ A_{13} = Nca_2 \cdot ica_2(t) + Nca_3 \cdot ica_3(t) \end{cases} \quad (2)$$

Considering that the auxiliary windings are series connected and the secondary currents are flowing through it, (3) one obtains:

$$\begin{cases} ia_1(t) = ibc_4(t) = iab_2(t) \\ ia_2(t) = ica_1(t) = ibc_3(t) \\ ib_1(t) = ica_4(t) = ibc_2(t) \end{cases}$$
$$\begin{cases} ib_2(t) = iab_1(t) = ica_3(t) \\ ic_1(t) = iab_4(t) = ica_2(t) \\ ic_2(t) = ibc_1(t) = iab_3(t) \end{cases} \quad (3)$$

Substituting (1) and (2) in (3) yields:

$$\begin{cases} Nab \cdot iab(t) + Nab_1 \cdot ib_2(t) + Nab_4 \cdot ic_1(t) = A_{14} \\ Nbc \cdot ibc(t) + Nbc_1 \cdot ic_2(t) + Nbc_4 \cdot ia_1(t) = A_{15} \\ Nca \cdot ica(t) + Nca_1 \cdot ia_2(t) + Nca_4 \cdot ib_1(t) = A_{16} \end{cases} \quad (4)$$

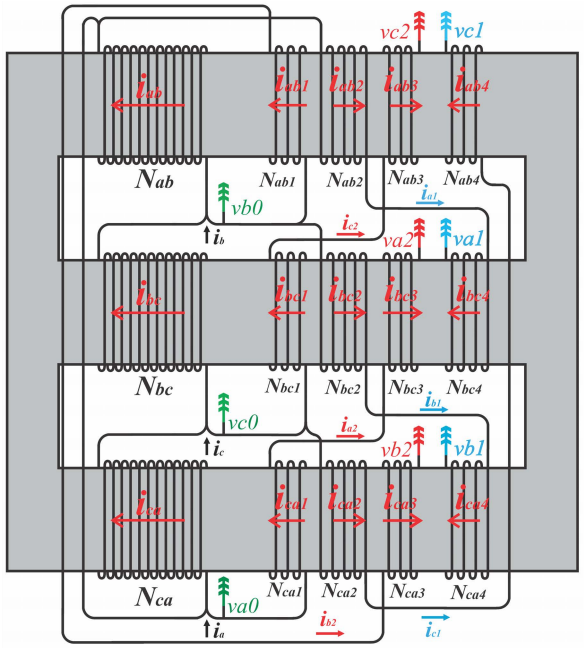

FIGURE 3. Illustration of the windings on a three-limb core.

where:

$$\begin{cases} A_{14} = Nab_2 \cdot ia_1(t) + Nab_3 \cdot ic_2(t) \\ A_{15} = Nbc_2 \cdot ib_1(t) + Nbc_3 \cdot ia_2(t) \\ A_{16} = Nca_2 \cdot ic_1(t) + Nca_3 \cdot ib_2(t) \end{cases} \tag{5}$$

Therefore, *iab(t)*, *ibc(t)*, and *ica(t)* can be given by (6):

$$\begin{cases} iab(t) = \dfrac{A_{17} - A_{18}}{Nab} \\ ibc(t) = \dfrac{A_{19} - A_{20}}{Nbc} \\ ica(t) = \dfrac{A_{21} - A_{22}}{Nca} \end{cases} \tag{6}$$

being that:

$$\begin{cases} A_{17} = Nab_2 \cdot ia_1(t) + Nab_3 \cdot ic_2(t) \\ A_{18} = Nab_1 \cdot ib_2(t) - Nab_4 \cdot ic_1(t) \\ A_{19} = Nbc_2 \cdot ib_1(t) + Nbc_3 \cdot ia_2(t) \\ A_{20} = Nbc_1 \cdot ic_2(t) - Nbc_4 \cdot ia_1(t) \\ A_{21} = Nca_2 \cdot ic_1(t) + Nca_3 \cdot ib_2(t) \\ A_{22} = Nca_1 \cdot ia_2(t) - Nca_4 \cdot ib_1(t) \end{cases} \tag{7}$$

With the understanding that:

$$\begin{cases} Nab = Nbc = Nca \\ Nab_1 = Nab_2 = Nbc_1 = Nbc_2 = Nca_1 = Nca_2 \\ Nab_3 = Nab_4 = Nbc_3 = Nbc_4 = Nca_3 = Nca_4 \end{cases} \tag{8}$$

Thus, the voltage gains concerning the auxiliary windings are given by:

$$\begin{cases} K_b = \dfrac{Nab}{Nab_1} = \dfrac{Nbc}{Nbc_1} = \dfrac{Nca}{Nca_1} \\ K_c = \dfrac{Nab}{Nab_3} = \dfrac{Nbc}{Nbc_3} = \dfrac{Nca}{Nca_3} \end{cases} \tag{9}$$

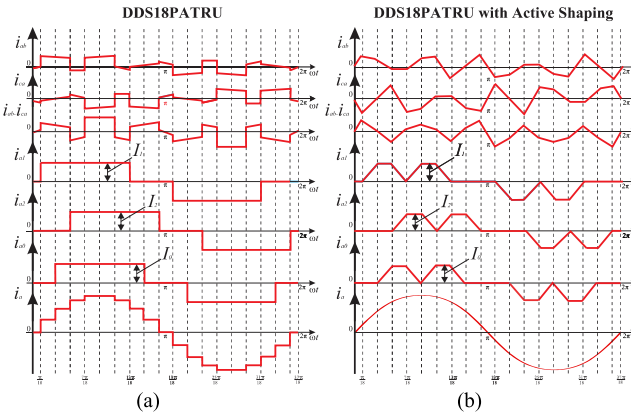

FIGURE 4. Input line current composition, line A for example (a) 18-pulse operation (b) active current shaping operation.

Substituting (8) and (9) in (6) yields

$$\begin{cases} iab(t) = \dfrac{ia_1(t) - ib_2(t)}{K_b} + \dfrac{ic_2(t) - ic_1(t)}{K_c} \\ ibc(t) = \dfrac{ib_1(t) - ic_2(t)}{K_b} + \dfrac{ia_2(t) - ia_1(t)}{K_c} \\ ica(t) = \dfrac{ic_1(t) - ia_2(t)}{K_b} + \dfrac{ib_2(t) - ib_1(t)}{K_c} \end{cases} \tag{10}$$

From Kirchhoff's current law, the primary input line currents are given by (11).

$$\begin{cases} ia(t) = ia_1(t) + ia_2(t) + ia_0(t) + iab(t) - ica(t) \\ ib(t) = ib_1(t) + ib_2(t) + ib_0(t) + ibc(t) - iab(t) \\ ic(t) = ic_1(t) + ic_2(t) + ic_0(t) + ica(t) - ibc(t) \end{cases} \tag{11}$$

Substituting (10) in (11) yields

$$\begin{cases} ia(t) = ia_1(t) + ia_2(t) + ia_0(t) + A_{23} + A_{24} \\ ib(t) = ib_1(t) + ib_2(t) + ib_0(t) + A_{25} + A_{26} \\ ic(t) = ic_1(t) + ic_2(t) + ic_0(t) + A_{27} + A_{28} \end{cases} \tag{12}$$

being that:

$$\begin{cases} A_{23} = \dfrac{ia_1(t) + ia_2(t) - ib_2(t) - ic_1(t)}{K_b} \\ A_{24} = \dfrac{ib_1(t) + ic_2(t) - ib_2(t) - ic_1(t)}{K_c} \\ A_{25} = \dfrac{ib_1(t) + ib_2(t) - ia_1(t) - ic_2(t)}{K_b} \\ A_{26} = \dfrac{ia_2(t) + ic_1(t) - ia_1(t) - ic_2(t)}{K_c} \\ A_{27} = \dfrac{ic_1(t) + ic_2(t) - ia_2(t) - ib_1(t)}{K_b} \\ A_{28} = \dfrac{ia_1(t) + ib_2(t) - ia_2(t) - ib_1(t)}{K_c} \end{cases} \tag{13}$$

According to (12) and (13), the theoretical waveform of the input line current *ia* is obtained as shown in Fig. 4, where one notes that the input line current exhibits 18-step waves in one power supply cycle.

B. DDS18PATRU: DETERMINATION OF THE VOLTAGE MAGNITUDE ACROSS THE AUXILIARY WINDINGS FOR OPERATION WITH UNITARY VOLTAGE GAIN

In Fig. 2(b), the voltages *va0, vb0* and *vc0* correspond to the secondary voltages, which are in phase with the mains supply voltages *va, vb,* and *vc*, thus maintaining the magnitude of secondary voltages the same as the original primary voltage ($Va = Va0 = 115V$). The magnitude of phasor Vaux, which represents the voltage between a neutral point and the auxiliary windings, has the purpose of obtaining the voltage on the windings.

According to the triangle composed by phasor voltages *Vaux, Vab2* and *Va*, it is easy to obtain the trigonometric function relationship of the input voltages for each DBRU. As an example, for phase A, this is given by (14):

$$v_{xy} = v_x \cdot \frac{sin\left(\frac{\pi}{6}\right)}{sin\left(\frac{5\pi}{6} - \alpha\right)} \cdot \frac{sin\left(\frac{\pi}{2} - \alpha\right)}{sin\left(\frac{11\pi}{18}\right)} \tag{14}$$

where:

$$\alpha = -atan\left[\frac{\sqrt{3}}{3} \cdot \left(\frac{115 \cdot G \cdot cos\left(\frac{\pi}{9}\right) - 115}{115 \cdot G \cdot cos\left(\frac{\pi}{9}\right)}\right)\right] \tag{15}$$

It is worth mentioning that the gain G corresponds to the global voltage gain of the autotransformer (between input and output voltages), while *Kb* and *Kc* used in (10) and (13) correspond to the voltage gains concerning the auxiliary windings of the autotransformer.

Therefore, the magnitude of phasor Vxx1,2 which represents the voltage between a neutral point and the auxiliary windings is given by (16).

$$v_{xx1,2} = v_x \cdot \frac{sin\left(\frac{\pi}{6}\right)}{sin\left(\frac{5\pi}{6} - \alpha\right)} \cdot \frac{sin\left(\alpha\right)}{sin\left(\frac{\pi}{6}\right)} \tag{16}$$

The magnitude of phasors Vxx3,4, which are the auxiliary windings, is given by (17).

$$v_{xx3,4} = v_x \cdot \frac{sin\left(\frac{\pi}{6}\right)}{sin\left(\frac{5\pi}{6} - \alpha\right)} \cdot \frac{sin\left(\alpha - \frac{\pi}{9}\right)}{sin\left(\frac{11\pi}{18}\right)} \tag{17}$$

C. DDS18PATRU: THEORETICAL WAVEFORM OF INPUT LINE CURRENT WITHOUT ACTIVE SHAPING

From the analysis of the theoretical waveforms portrayed in Fig. 4(a), the windings currents and the ac grid current can be expressed by its respective Fourier series given by (18), where the coefficient k is the number of harmonic iterations.

By the Fourier series, the greater the number of iterations, the more graphically accurate are the waveforms obtained. Therefore, using mathematical calculation softwares such as Mathcad® and Mathcad Prime®, the analysis of the autotransformer's input and output currents without active shaping was performed considering up to the 37th harmonic component.

$$\begin{cases} ia_0(t) = \frac{2\sqrt{3}}{3\pi} \cdot Id \cdot \left(\frac{1}{1 - D_{boost}}\right) \\ \quad \cdot (\sin(\omega t) - B_{11} + B_{12}) \\ ia_1(t) = \frac{2\sqrt{3}}{3\pi} \cdot Id \cdot \left(\frac{1}{1 - D_{boost}}\right) \\ \quad \cdot \left(\sin\left(\omega t + \frac{\pi}{9}\right) - B_{13} + B_{14}\right) \\ ia_2(t) = \frac{2\sqrt{3}}{3\pi} \cdot Id \cdot \left(\frac{1}{1 - D_{boost}}\right) \\ \quad \cdot \left(\sin\left(\omega t - \frac{\pi}{9}\right) - B_{15} + B_{16}\right) \end{cases}$$

$$\begin{cases} ib_0(t) = \frac{2\sqrt{3}}{3\pi} \cdot Id \cdot \left(\frac{1}{1 - D_{boost}}\right) \\ \quad \cdot \left(\sin\left(\omega t + \frac{2\pi}{3}\right) - B_{17} + B_{18}\right) \\ ib_1(t) = \frac{2\sqrt{3}}{3\pi} \cdot Id \cdot \left(\frac{1}{1 - D_{boost}}\right) \\ \quad \cdot \left(\sin\left(\omega t + \frac{7\pi}{9}\right) - B_{19} + B_{20}\right) \\ ib_2(t) = \frac{2\sqrt{3}}{3\pi} \cdot Id \cdot \left(\frac{1}{1 - D_{boost}}\right) \\ \quad \cdot \left(\sin\left(\omega t + \frac{5\pi}{9}\right) - B_{21} + B_{22}\right) \end{cases}$$

$$\begin{cases} ic_0(t) = \frac{2\sqrt{3}}{3\pi} \cdot Id \cdot \left(\frac{1}{1 - D_{boost}}\right) \\ \quad \cdot \left(\sin\left(\omega t - \frac{2\pi}{3}\right) - B_{23} + B_{24}\right) \\ ic_1(t) = \frac{2\sqrt{3}}{3\pi} \cdot Id \cdot \left(\frac{1}{1 - D_{boost}}\right) \\ \quad \cdot \left(\sin\left(\omega t - \frac{5\pi}{9}\right) - B_{25} + B_{26}\right) \\ ic_2(t) = \frac{2\sqrt{3}}{3\pi} \cdot Id \cdot \left(\frac{1}{1 - D_{boost}}\right) \\ \quad \cdot \left(\sin\left(\omega t - \frac{7\pi}{9}\right) - B_{27} + B_{28}\right) \end{cases}$$

$$\begin{cases} ia(t) = \frac{2\sqrt{3}}{\pi} \cdot Id \cdot \left(\frac{1}{1 - D_{boost}}\right) \\ \quad \cdot (\sin(\omega t) - B_{29} + B_{30}) \\ ib(t) = \frac{2\sqrt{3}}{\pi} \cdot Id \cdot \left(\frac{1}{1 - D_{boost}}\right) \\ \quad \cdot \left(\sin\left(\omega t + \frac{2\pi}{3}\right) - B_{31} + B_{32}\right) \\ ic(t) = \frac{2\sqrt{3}}{\pi} \cdot Id \cdot \left(\frac{1}{1 - D_{boost}}\right) \\ \quad \cdot \left(\sin\left(\omega t - \frac{2\pi}{3}\right) - B_{33} + B_{34}\right) \end{cases} \tag{18}$$

being that:

$$
\begin{cases}
B_{11} = \sum_{k=5,7,17,19\ldots} \frac{1}{k} \cdot \sin\left(k \cdot \omega t\right) \\
B_{12} = \sum_{k=11,13,23,25\ldots} \frac{1}{k} \cdot \sin\left(k \cdot \omega t\right) \\
B_{13} = \sum_{k=5,7,17,19\ldots} \frac{1}{k} \cdot \sin\left(k \cdot \left(\omega t + \frac{\pi}{9}\right)\right) \\
B_{14} = \sum_{k=11,13,23,25\ldots} \frac{1}{k} \cdot \sin\left(k \cdot \left(\omega t + \frac{\pi}{9}\right)\right) \\
B_{15} = \sum_{k=5,7,17,19\ldots} \frac{1}{k} \cdot \sin\left(k \cdot \left(\omega t - \frac{\pi}{9}\right)\right) \\
B_{16} = \sum_{k=11,13,23,25\ldots} \frac{1}{k} \cdot \sin\left(k \cdot \left(\omega t - \frac{\pi}{9}\right)\right)
\end{cases}
$$

$$
\begin{cases}
B_{17} = \sum_{k=5,7,17,19\ldots} \frac{1}{k} \cdot \sin\left(k \cdot \left(\omega t + \frac{2\pi}{3}\right)\right) \\
B_{18} = \sum_{k=11,13,23,25\ldots} \frac{1}{k} \cdot \sin\left(k \cdot \left(\omega t + \frac{2\pi}{3}\right)\right) \\
B_{19} = \sum_{k=5,7,17,19\ldots} \frac{1}{k} \cdot \sin\left(k \cdot \left(\omega t + \frac{7\pi}{9}\right)\right) \\
B_{20} = \sum_{k=11,13,23,25\ldots} \frac{1}{k} \cdot \sin\left(k \cdot \left(\omega t + \frac{7\pi}{9}\right)\right) \\
B_{21} = \sum_{k=5,7,17,19\ldots} \frac{1}{k} \cdot \sin\left(k \cdot \left(\omega t + \frac{5\pi}{9}\right)\right) \\
B_{22} = \sum_{k=11,13,23,25\ldots} \frac{1}{k} \cdot \sin\left(k \cdot \left(\omega t + \frac{5\pi}{9}\right)\right)
\end{cases}
$$

$$
\begin{cases}
B_{23} = \sum_{k=5,7,17,19\ldots} \frac{1}{k} \cdot \sin\left(k \cdot \left(\omega t - \frac{2\pi}{3}\right)\right) \\
B_{24} = \sum_{k=11,13,23,25\ldots} \frac{1}{k} \cdot \sin\left(k \cdot \left(\omega t - \frac{2\pi}{3}\right)\right) \\
B_{25} = \sum_{k=5,7,17,19\ldots} \frac{1}{k} \cdot \sin\left(k \cdot \left(\omega t - \frac{5\pi}{9}\right)\right) \\
B_{26} = \sum_{k=11,13,23,25\ldots} \frac{1}{k} \cdot \sin\left(k \cdot \left(\omega t - \frac{5\pi}{9}\right)\right) \\
B_{27} = \sum_{k=5,7,17,19\ldots} \frac{1}{k} \cdot \sin\left(k \cdot \left(\omega t - \frac{7\pi}{9}\right)\right) \\
B_{28} = \sum_{k=11,13,23,25\ldots} \frac{1}{k} \cdot \sin\left(k \cdot \left(\omega t - \frac{7\pi}{9}\right)\right)
\end{cases}
$$

$$
\begin{cases}
B_{29} = \sum_{k=17,19\ldots} \frac{1}{k} \cdot \sin\left(k \cdot (\omega t)\right) \\
B_{30} = \sum_{k=35,37\ldots} \frac{1}{k} \cdot \sin\left(k \cdot \omega t\right) \\
B_{31} = \sum_{k=17,19\ldots} \frac{1}{k} \cdot \sin\left(k \cdot \left(\omega t + \frac{2\pi}{3}\right)\right) \\
B_{32} = \sum_{k=35,37\ldots} \frac{1}{k} \cdot \sin\left(k \cdot \left(\omega t + \frac{2\pi}{3}\right)\right) \\
B_{33} = \sum_{k=17,19\ldots} \frac{1}{k} \cdot \sin\left(k \cdot \left(\omega t - \frac{2\pi}{3}\right)\right) \\
B_{34} = \sum_{k=35,37\ldots} \frac{1}{k} \cdot \sin\left(k \cdot \left(\omega t - \frac{2\pi}{3}\right)\right)
\end{cases}
\tag{19}
$$

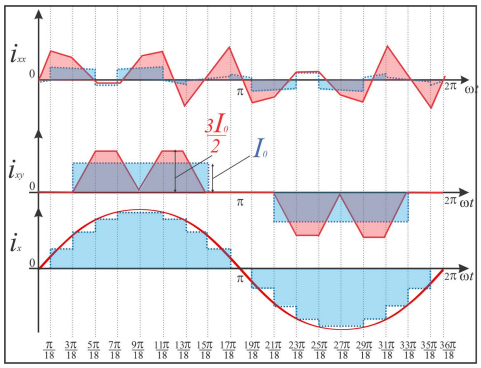

FIGURE 5. Comparison between the current waveforms circulating in the DDS18PATRU with active shaping (red) and without active shaping (blue).

Considering that the input inductor current of each Boost converter is given by (20), as shown at the bottom of the next page, where Id is the rated load current and *Dboost* is the duty cycle, the RMS value of the windings current can be obtained by (21), as shown at the bottom of the next page. Hence, the RMS value of the ac grid currents can be given by (22), as shown at the bottom of the next page. Therefore, finding the RMS values given by (21) and (22), the current flowing through the main coils *Nab, Nbc,* and *Nca* can be determined using (10).

D. DDS-18PATRU: THEORETICAL WAVEFORM OF INPUT LINE CURRENT WITH ACTIVE SHAPING

From the analysis of the theoretical waveforms portrayed in Figs. 4 and 5, one reaches the conclusion that with the active current shaping, the area of the auxiliary winding currents is reduced by about 33% in a half cycle, which would decrease the RMS values, and hence reduce the power transferred to the load. To compensate for this difference and supply the power required by the load with the desired THDi, the value of the peak currents flowing through the auxiliary windings of the DDS18PATRU are increased by almost 50%, thus raising the RMS values by about 10%. Therefore, the primary coils *Nab, Nca* and *Nbc* are those that suffer the greatest increase in the current values since the RMS current values are increased by almost 80%.

Focusing the analysis on the waveform of the currents imposed on the auxiliary windings, as illustrated in Fig. 6, it is possible to obtain (23), as shown at the bottom of page 9. Hence, the respective Fourier series is given by (24), as shown at the bottom of page 10, where the coefficients *an* and *bn* of the periodic functions of the auxiliary winding currents are given by (25), as shown at the bottom of page 11. With (24) and (25) at hand, it is necessary to perform about a thousand mathematical iterations to obtain, with suitable precision, the equations of currents in the time domain, which are given by (26) and (27), as shown at the bottom of page 12. Therefore, it is possible to determine the kVA rating of the

DDS-18PATRU operating with active shaping, as demonstrated in the next section.

Finally, from the equations of currents in the time domain given by (26), the RMS value of the currents drawn from the grid are obtained by (27).

E. DDS-18PATRU: DETERMINATION OF THE kVA RATING WITH AND WITHOUT ACTIVE CURRENT SHAPING

With (26) and (27) at hand, and in the knowledge that the RMS value of the currents on the windings of the DDS18PATRU can be obtained through (28), the RMS value

$$I_0 = I_1 = I_2 = \frac{Id}{3} \cdot \left(\frac{1}{1 - D_{boost}}\right) \tag{20}$$

$$\begin{cases} ia_{0(rms)} = \sqrt{\frac{1}{T}\int_0^T \left[\frac{2\sqrt{3}}{3\pi} \cdot Id \cdot \left(\frac{1}{1 - D_{boost}}\right) \cdot (\sin(\omega t) - B_{11} + B_{12})\right]^2 dt} \\ ia_{1(rms)} = \sqrt{\frac{1}{T}\int_0^T \left[\frac{2\sqrt{3}}{3\pi} \cdot Id \cdot \left(\frac{1}{1 - D_{boost}}\right) \cdot \left(\sin\left(\omega t + \frac{\pi}{9}\right) - B_{13} + B_{14}\right)\right]^2 dt} \\ ia_{2(rms)} = \sqrt{\frac{1}{T}\int_0^T \left[\frac{2\sqrt{3}}{3\pi} \cdot Id \cdot \left(\frac{1}{1 - D_{boost}}\right) \cdot \left(\sin\left(\omega t - \frac{\pi}{9}\right) - B_{15} + B_{16}\right)\right]^2 dt} \end{cases}$$

$$\begin{cases} ib_{0(rms)} = \sqrt{\frac{1}{T}\int_0^T \left[\frac{2\sqrt{3}}{3\pi} \cdot Id \cdot \left(\frac{1}{1 - D_{boost}}\right) \cdot \left(\sin\left(\omega t + \frac{2\pi}{3}\right) - B_{17} + B_{18}\right)\right]^2 dt} \\ ib_{1(rms)} = \sqrt{\frac{1}{T}\int_0^T \left[\frac{2\sqrt{3}}{3\pi} \cdot Id \cdot \left(\frac{1}{1 - D_{boost}}\right) \cdot \left(\sin\left(\omega t + \frac{7\pi}{9}\right) - B_{19} + B_{20}\right)\right]^2 dt} \\ ib_{2(rms)} = \sqrt{\frac{1}{T}\int_0^T \left[\frac{2\sqrt{3}}{3\pi} \cdot Id \cdot \left(\frac{1}{1 - D_{boost}}\right) \cdot \left(\sin\left(\omega t + \frac{5\pi}{9}\right) - B_{21} + B_{22}\right)\right]^2 dt} \end{cases} \tag{21}$$

$$\begin{cases} ic_{0(rms)} = \sqrt{\frac{1}{T}\int_0^T \left[\frac{2\sqrt{3}}{3\pi} \cdot Id \cdot \left(\frac{1}{1 - D_{boost}}\right) \cdot \left(\sin\left(\omega t - \frac{2\pi}{3}\right) - B_{23} + B_{24}\right)\right]^2 dt} \\ ic_{1(rms)} = \sqrt{\frac{1}{T}\int_0^T \left[\frac{2\sqrt{3}}{3\pi} \cdot Id \cdot \left(\frac{1}{1 - D_{boost}}\right) \cdot \left(\sin\left(\omega t - \frac{5\pi}{9}\right) - B_{25} + B_{26}\right)\right]^2 dt} \\ ic_{2(rms)} = \sqrt{\frac{1}{T}\int_0^T \left[\frac{2\sqrt{3}}{3\pi} \cdot Id \cdot \left(\frac{1}{1 - D_{boost}}\right) \cdot \left(\sin\left(\omega t - \frac{7\pi}{9}\right) - B_{27} + B_{28}\right)\right]^2 dt} \end{cases}$$

$$\begin{cases} ia_{(rms)} = \sqrt{\frac{1}{T}\int_0^T \left[\frac{2\sqrt{3}}{\pi} \cdot Id \cdot \left(\frac{1}{1 - D_{boost}}\right) \cdot (\sin(\omega t) - B_{29} + B_{30})\right] dt} \\ ib_{(rms)} = \sqrt{\frac{1}{T}\int_0^T \left[\frac{2\sqrt{3}}{\pi} \cdot Id \cdot \left(\frac{1}{1 - D_{boost}}\right) \cdot \left(\sin\left(\omega t + \frac{2\pi}{3}\right) - B_{31} + B_{32}\right)\right] dt} \\ ic_{(rms)} = \sqrt{\frac{1}{T}\int_0^T \left[\frac{2\sqrt{3}}{\pi} \cdot Id \cdot \left(\frac{1}{1 - D_{boost}}\right) \cdot \left(\sin\left(\omega t - \frac{2\pi}{3}\right) - B_{33} + B_{34}\right)\right] dt} \end{cases} \tag{22}$$

of the currents on each winding can be found using (29), which is obtained as a function of the output current at rated load (Id).

$$ixy(rms) = \sqrt{\frac{1}{T} \cdot \int_0^T (ixy(t))^2 \, dt} \tag{28}$$

$$\begin{cases} ixy_{(rms)} = 0.27 \cdot Id \cdot \left(\dfrac{1}{1 - Dboost}\right) \\ ixx_{(rms)} = 0.034 \cdot Id \cdot \left(\dfrac{1}{1 - Dboost}\right) \end{cases} \tag{29}$$

For a generic voltage gain condition, 6 more coils are added for voltage regulation V_{x0}, and (17) can be rewritten as follows:

$$v_{xxn} = \frac{115 \cdot G - 115}{2 \cdot \cos\left(\frac{\pi}{6}\right)} \tag{30}$$

where G is the DDS-18PATRU global voltage gain.

If the average output voltage across each DBRU terminals is calculated by (31), as shown at the bottom of page 13, the kVA rating is given by (32), as shown at the bottom of page 13.

Substituting (14)-(17) and (29)-(31) into (32), the general equation of the kVA rating of the autotransformer as a function of voltage gain (G) can be given by (33), as shown at the bottom of page 13, which is 16.82% when operating without active shaping.

Operating with active shaping, the peak value of the input inductor current of each Boost converter is increased. This elevation must be taken into account for the correct calculation of RMS currents. Therefore, with (34), as shown at the bottom of page 13, at hand, the new kVA rating is obtained by (35), as shown at the bottom of page 13, which is 21.03%.

Finally, through (32), one can evaluate the kVA rating for different values of voltage gain, as illustrated in Fig. 7. Therefore, one can conclude that, for unitary voltage gain,

$$\begin{cases} 0, 0 < x1 < {}^{\pi}/_{6} \\ \dfrac{Id \cdot \left(\frac{1}{1-D_{Boost}}\right)}{2\pi} \cdot (6 \cdot t - \pi), {}^{\pi}/_{6} < x2 < {}^{5\pi}/_{18} \\ \dfrac{Id}{3} \cdot \left(\dfrac{1}{1 - D_{Boost}}\right), {}^{5\pi}/_{6} < x3 < {}^{7\pi}/_{18} \\ \dfrac{3 \cdot Id \cdot \left(\frac{1}{1-D_{Boost}}\right)}{2\pi} \cdot (-2 \cdot t + \pi), {}^{7\pi}/_{6} < x4 < {}^{\pi}/_{2} \\ \dfrac{3 \cdot Id \cdot \left(\frac{1}{1-D_{Boost}}\right)}{2\pi} \cdot (2 \cdot t - \pi), {}^{\pi}/_{2} < x5 < {}^{11\pi}/_{18} \\ \dfrac{Id}{3} \cdot \left(\dfrac{1}{1 - D_{Boost}}\right), {}^{11\pi}/_{18} < x6 < {}^{13\pi}/_{18} \\ \dfrac{Id \cdot \left(\frac{1}{1-D_{Boost}}\right)}{2\pi} \cdot (-6 \cdot t + 5 \cdot \pi), {}^{13\pi}/_{18} < x7 < {}^{5\pi}/_{6} \\ 0, {}^{5\pi}/_{6} < x8 < {}^{7\pi}/_{6} \\ \dfrac{Id \cdot \left(\frac{1}{1-D_{Boost}}\right)}{2\pi} \cdot (-6 \cdot t + 7 \cdot \pi), {}^{7\pi}/_{6} < x9 < {}^{23\pi}/_{18} \\ -\dfrac{Id}{3} \cdot \left(\dfrac{1}{1 - D_{Boost}}\right), {}^{23\pi}/_{18} < x10 < {}^{25\pi}/_{18} \\ \dfrac{3 \cdot Id \cdot \left(\frac{1}{1-D_{Boost}}\right)}{2\pi} \cdot (2 \cdot t - 3 \cdot \pi), {}^{25\pi}/_{18} < x11 < {}^{3\pi}/_{2} \\ \dfrac{3 \cdot Id \cdot \left(\frac{1}{1-D_{Boost}}\right)}{2\pi} \cdot (-2 \cdot t + 3 \cdot \pi), {}^{3\pi}/_{2} < x12 < {}^{29\pi}/_{18} \\ -\dfrac{Id}{3} \cdot \left(\dfrac{1}{1 - D_{Boost}}\right), {}^{29\pi}/_{18} < x13 < {}^{31\pi}/_{18} \\ \dfrac{Id \cdot \left(\frac{1}{1-D_{Boost}}\right)}{2\pi} \cdot (6 \cdot t - 11 \cdot \pi), {}^{31\pi}/_{18} < x14 < {}^{11\pi}/_{6} \\ 0, {}^{11\pi}/_{6} < x15 < 2\pi \end{cases} \tag{23}$$

increasing the DDS-18PATRUs' kVA rating to around 4.21%, the proposed RU-DDS18PATR+Boost operates in accordance with the harmonic content restrictions imposed by the DO-160F standard.

In Fig. 7, special attention is also given to the results presented in [25] where the authors analyzed the transformers' kVA rating and the overall voltage gain G of various structures of 18-Pulse ATRUs (symmetric and asymmetric). It demonstrates that the DDS-18PATRU is the one with the lowest kVA rating, even with active current shaping, and for the voltage gain G ranging from 0.8 to 1.4.

F. DDS-18PATRU: CORE DESIGN AND SPECIFICATION

For MEA applications, one of the main concerns is to reduce the weight and volume of the rectifier unity. Therefore, the magnetic core material chosen for the implementation of the DDS-18PATRU is silicon steel. Compared to the amorphous core, it has more advantages in terms of noise, cost, saturation flux density and power density in applications with high power and medium frequency range [34].

The guideline design presented herein is based on the Ap method [35], where Ap is given by:

$$A_p = \frac{S_{total} \cdot 10^4}{Kf \cdot Ku \cdot Bm \cdot f \cdot J} \tag{36}$$

where $Stotal$ is the total power processed by the core (kVA rate), Kf is the waveform coefficient, Ku denotes the window utilization factor, Bm is the maximum flux density, f represents the operating frequency, and J is the current density.

The area occupied by the windings (Aw) is used to select the AWG of the wires according to (37). The highest losses are concentrated in iron and copper. Therefore, with the RMS value of the currents drawn from the grid given by (27), the optimal windings resistances can be determined by (38) and core losses can be determined by (39).

$$\begin{cases} A_{wp} = \dfrac{K_u \cdot W_a}{10 \cdot N_p} \\ A_{ws1} = \dfrac{K_u \cdot W_a}{10 \cdot N_{s1}} \\ A_{ws2} = \dfrac{K_u \cdot W_a}{10 \cdot N_{s2}} \end{cases} \tag{37}$$

$$\begin{cases} P_{prim} = 3 \cdot (I_{xx})^2 \cdot R_{prim} \\ P_{aux1} = 6 \cdot \left(I_{xy}\right)^2 \cdot R_{aux1} \\ P_{aux2} = 6 \cdot \left(I_{xy}\right)^2 \cdot R_{aux2} \end{cases} \tag{38}$$

$$P_{Cu} = P_{prim} + P_{aux1} + P_{aux2} \tag{39}$$

Finally, the iron losses can be determined by (40).

$$P_{Fe} = Watts/ki\log ram \cdot (W_e) \tag{40}$$

$$\begin{cases} ia_0(t) = \dfrac{I_d \cdot \left(\frac{1}{1-Dboost}\right)}{2\pi^2} \displaystyle\sum_{k=1}^{\infty} \left(\left(\sum_{n=1}^{12} a_n \right) \cdot \cos(k \cdot \omega \cdot t) + \left(\sum_{n=1}^{12} b_n \right) \cdot \sin(k \cdot \omega \cdot t) \right) \\ ia_1(t) = ia_0(t) = \dfrac{I_d \cdot \left(\frac{1}{1-Dboost}\right)}{2\pi^2} \displaystyle\sum_{k=1}^{\infty} \left(\left(\sum_{n=1}^{12} a_n \right) \cdot \cos\left(k \cdot \left(\omega t + \frac{\pi}{9}\right)\right) + \left(\sum_{n=1}^{12} b_n \right) \cdot \sin\left(k \cdot \left(\omega t + \frac{\pi}{9}\right)\right) \right) \\ ia_2(t) = ia_0(t) = \dfrac{I_d \cdot \left(\frac{1}{1-Dboost}\right)}{2\pi^2} \displaystyle\sum_{k=1}^{\infty} \left(\left(\sum_{n=1}^{12} a_n \right) \cdot \cos\left(k \cdot \left(\omega t - \frac{\pi}{9}\right)\right) + \left(\sum_{n=1}^{12} b_n \right) \cdot \sin\left(k \cdot \left(\omega t - \frac{\pi}{9}\right)\right) \right) \end{cases}$$

$$\begin{cases} ib_0(t) = \dfrac{I_d \cdot \left(\frac{1}{1-Dboost}\right)}{2\pi^2} \displaystyle\sum_{k=1}^{\infty} \left(\left(\sum_{n=1}^{12} a_n \right) \cdot \cos\left(k \cdot \left(\omega t + \frac{2\pi}{3}\right)\right) + \left(\sum_{n=1}^{12} b_n \right) \cdot \sin\left(k \cdot \left(\omega t + \frac{2\pi}{3}\right)\right) \right) \\ ib_1(t) = \dfrac{I_d \cdot \left(\frac{1}{1-Dboost}\right)}{2\pi^2} \displaystyle\sum_{k=1}^{\infty} \left(\left(\sum_{n=1}^{12} a_n \right) \cdot \cos\left(k \cdot \left(\omega t + \frac{7\pi}{9}\right)\right) + \left(\sum_{n=1}^{12} b_n \right) \cdot \sin\left(k \cdot \left(\omega t + \frac{7\pi}{9}\right)\right) \right) \\ ib_2(t) = \dfrac{I_d \cdot \left(\frac{1}{1-Dboost}\right)}{2\pi^2} \displaystyle\sum_{k=1}^{\infty} \left(\left(\sum_{n=1}^{12} a_n \right) \cdot \cos\left(k \cdot \left(\omega t + \frac{5\pi}{9}\right)\right) + \left(\sum_{n=1}^{12} b_n \right) \cdot \sin\left(k \cdot \left(\omega t + \frac{5\pi}{9}\right)\right) \right) \end{cases}$$

$$\begin{cases} ic_0(t) = \dfrac{I_d \cdot \left(\frac{1}{1-Dboost}\right)}{2\pi^2} \displaystyle\sum_{k=1}^{\infty} \left(\left(\sum_{n=1}^{12} a_n \right) \cdot \cos\left(k \cdot \left(\omega t - \frac{2\pi}{3}\right)\right) + \left(\sum_{n=1}^{12} b_n \right) \cdot \sin\left(k \cdot \left(\omega t - \frac{2\pi}{3}\right)\right) \right) \\ ic_1(t) = \dfrac{I_d \cdot \left(\frac{1}{1-Dboost}\right)}{2\pi^2} \displaystyle\sum_{k=1}^{\infty} \left(\left(\sum_{n=1}^{12} a_n \right) \cdot \cos\left(k \cdot \left(\omega t - \frac{5\pi}{9}\right)\right) + \left(\sum_{n=1}^{12} b_n \right) \cdot \sin\left(k \cdot \left(\omega t - \frac{5\pi}{9}\right)\right) \right) \\ ic_2(t) = \dfrac{I_d \cdot \left(\frac{1}{1-Dboost}\right)}{2\pi^2} \displaystyle\sum_{k=1}^{\infty} \left(\left(\sum_{n=1}^{12} a_n \right) \cdot \cos\left(k \cdot \left(\omega t - \frac{7\pi}{9}\right)\right) + \left(\sum_{n=1}^{12} b_n \right) \cdot \sin\left(k \cdot \left(\omega t - \frac{7\pi}{9}\right)\right) \right) \end{cases} \tag{24}$$

To conclude, in Tab. 2 the specification of the DDS-18PATRU implemented in the laboratory and used for experimental analysis is presented. The insulation design of the five windings in each window of the DDS-18PATRU was established based on IEC 60076-11:2004. It corresponds to the standard for dry-type power transformers and establishes the use of class F materials that resist maximum temperature of up to 155° and an insulation voltage of up to 1.1kV [36].

III. BOOST CONVERTER: DESIGN, SPECIFICATION AND CONTROL STRATEGY

Through the employment of the DDS-18PATRU with cascaded dc-dc converters with input current source characteristics, the conclusion is reached that the imposition of currents with trapezoidal waveform and a frequency of 2400Hz to 4800Hz on the input inductors of each Boost converter, as portrayed in Fig. 8 (Iy-ref = $I_{1\text{-ref}}$, $I_{2\text{-ref}}$, $I_{3\text{-ref}}$ shown in Fig. 9), opens the possibility for obtaining perfectly sinusoidal currents on the supply grid. Taking $I_{1\text{-ref}}$ as an example (also depicted in Fig. 1), this should be in phase with the line-to-line voltage ($V_{a1b1} = V_{xy}$ in Fig. 8) of DBRU-1, which should result in phase A, the ac current waveforms as illustrated in Fig. 4(b).

The Boost converter is a dc-dc converter with an input current source characteristic, allowing for a direct connection to the ATRU. In addition to contributing to the imposition of sinusoidal input line currents, it also allows for voltage regulation and connection with different loads. It is a converter with a simple and robust converter with a reduced number

$$
\begin{aligned}
a1 &= \frac{k\cdot\pi\cdot\sin\left(\frac{31\cdot k\cdot\pi}{18}\right)+9\cdot\cos\left(\frac{11\cdot k\cdot\pi}{6}\right)-9\cdot\cos\left(\frac{31\cdot k\cdot\pi}{6}\right)}{k^2}\\
b1 &= \frac{9\cdot\sin\left(\frac{11\cdot k\cdot\pi}{6}\right)-\left(9\cdot\sin\left(\frac{31\cdot k\cdot\pi}{18}\right)+k\cdot\pi\cdot\cos\left(\frac{31\cdot k\cdot\pi}{18}\right)\right)}{k^2}\\
a2 &= \frac{k\cdot\pi\cdot\sin\left(\frac{25\cdot k\cdot\pi}{18}\right)-9\cdot\cos\left(\frac{25\cdot k\cdot\pi}{18}\right)}{k^2} \quad b2 = \frac{9\cdot I_0\cdot\sin\left(\frac{3\cdot k\cdot\pi}{2}\right)-\left(9\cdot I_0\cdot\sin\left(\frac{25\cdot k\cdot\pi}{18}\right)+k\cdot\pi\cdot\cos\left(\frac{25\cdot k\cdot\pi}{18}\right)\right)}{k^2}\\
a3 &= \frac{\sin\left(\frac{13\cdot k\cdot\pi}{18}\right)-\sin\left(\frac{11\cdot k\cdot\pi}{18}\right)}{k} \quad b3 = \frac{9\cdot\sin\left(\frac{11\cdot k\cdot\pi}{2}\right)-\left(9\cdot\sin\left(\frac{k\cdot\pi}{2}\right)+k\cdot\pi\cdot\cos\left(\frac{11\cdot k\cdot\pi}{18}\right)\right)}{k^2}\\
a4 &= \frac{k\cdot\pi\cdot\sin\left(\frac{11\cdot k\cdot\pi}{18}\right)+9\cdot\cos\left(\frac{11\cdot k\cdot\pi}{18}\right)}{k^2} \quad b4 = \frac{9\cdot\sin\left(\frac{5\cdot k\cdot\pi}{18}\right)-\left(9\cdot I_0\cdot\sin\left(\frac{k\cdot\pi}{6}\right)+k\cdot\pi\cdot\cos\left(\frac{5\cdot k\cdot\pi}{18}\right)\right)}{k^2}\\
a5 &= \frac{\sin\left(\frac{7\cdot k\cdot\pi}{18}\right)-\sin\left(\frac{5\cdot k\cdot\pi}{18}\right)}{k} \quad b5 = \frac{\cos\left(\frac{31\cdot k\cdot\pi}{18}\right)-\cos\left(\frac{29\cdot k\cdot\pi}{18}\right)}{k}\\
a6 &= \frac{k\cdot\pi\cdot\sin\left(\frac{5\cdot k\cdot\pi}{18}\right)+9\cdot\cos\left(\frac{5\cdot k\cdot\pi}{18}\right)-9\cdot\cos\left(\frac{k\cdot\pi}{6}\right)}{k^2} \quad b6 = \frac{\cos\left(\frac{25\cdot k\cdot\pi}{18}\right)-\cos\left(\frac{23\cdot k\cdot\pi}{18}\right)}{k}\\
a7 &= \frac{-k\cdot\pi\cdot\sin\left(\frac{7\cdot k\cdot\pi}{18}\right)-9\cdot\cos\left(\frac{7\cdot k\cdot\pi}{18}\right)}{k^2} \quad b7 = \frac{-\cos\left(\frac{13\cdot k\cdot\pi}{18}\right)+\cos\left(\frac{11\cdot k\cdot\pi}{18}\right)}{k}\\
a8 &= \frac{-k\cdot\pi\cdot\sin\left(\frac{13\cdot k\cdot\pi}{18}\right)+9\cdot\cos\left(\frac{5\cdot k\cdot\pi}{6}\right)-9\cdot\cos\left(\frac{13\cdot k\cdot\pi}{18}\right)}{k^2} \quad b8 = \frac{-\cos\left(\frac{7\cdot k\cdot\pi}{18}\right)+\cos\left(\frac{5\cdot k\cdot\pi}{18}\right)}{k}\\
a9 &= \frac{-k\cdot\pi\cdot\sin\left(\frac{23\cdot k\cdot\pi}{18}\right)+9\cdot\cos\left(\frac{23\cdot k\cdot\pi}{18}\right)-9\cdot\cos\left(\frac{7\cdot k\cdot\pi}{6}\right)}{k^2}\\
b9 &= \frac{-9\cdot\sin\left(\frac{k\cdot\pi}{2}\right)-\left(9\cdot\sin\left(\frac{7\cdot k\cdot\pi}{18}\right)+k\cdot\pi\cdot\cos\left(\frac{7\cdot k\cdot\pi}{18}\right)\right)}{k^2}\\
a10 &= \frac{-\sin\left(\frac{25\cdot k\cdot\pi}{18}\right)-\sin\left(\frac{23\cdot k\cdot\pi}{18}\right)}{k} \quad b10 = \frac{-9\cdot\sin\left(\frac{5\cdot k\cdot\pi}{6}\right)-\left(9\cdot\sin\left(\frac{13\cdot k\cdot\pi}{18}\right)+k\cdot\pi\cdot\cos\left(\frac{13\cdot k\cdot\pi}{18}\right)\right)}{k^2}\\
a11 &= \frac{-k\cdot\pi\cdot\sin\left(\frac{29\cdot k\cdot\pi}{18}\right)+9\cdot\cos\left(\frac{29\cdot k\cdot\pi}{18}\right)}{k^2} \quad b11 = \frac{-9\cdot\sin\left(\frac{23\cdot k\cdot\pi}{18}\right)-\left(9\cdot\sin\left(\frac{7\cdot k\cdot\pi}{6}\right)+k\cdot\pi\cdot\cos\left(\frac{23\cdot k\cdot\pi}{18}\right)\right)}{k^2}\\
a12 &= \frac{-\sin\left(\frac{31\cdot k\cdot\pi}{18}\right)-\sin\left(\frac{29\cdot k\cdot\pi}{18}\right)}{k} \quad b12 = \frac{-9\cdot\sin\left(\frac{29\cdot k\cdot\pi}{18}\right)-\left(9\cdot\sin\left(\frac{3\cdot k\cdot\pi}{2}\right)+k\cdot\pi\cdot\cos\left(\frac{29\cdot k\cdot\pi}{18}\right)\right)}{k^2}
\end{aligned}
\tag{25}
$$

of electronic components, contributing toward improving the overall efficiency of the structure. In addition, this converter does not require galvanic isolation. In the proposed RU, the Boost converter is designed to operate in continuous conduction mode with a duty-cycle (Dboost) equal to 0.505. Following the well-known design procedure presented in [37], the specifications for the deployed Boost converter are presented in Tab. 3.

$$\begin{cases}
ia_{0(rms)} = \sqrt{\frac{1}{T}\int_0^T \left[\frac{I_d\cdot\left(\frac{1}{1-Dboost}\right)}{2\pi^2}\sum_{k=1}^{\infty}\left(\left(\sum_{n=1}^{12}a_n\right)\cdot\cos(k\cdot\omega\cdot t)+\left(\sum_{n=1}^{12}b_n\right)\cdot\sin(k\cdot\omega\cdot t)\right)\right]^2 dt} \\
ia_{1(rms)} = \sqrt{\frac{1}{T}\int_0^T \left[\frac{I_d\cdot\left(\frac{1}{1-Dboost}\right)}{2\pi^2}\sum_{k=1}^{\infty}\left(\left(\sum_{n=1}^{12}a_n\right)\cdot\cos\left(k\cdot\left(\omega t+\frac{\pi}{9}\right)\right)+\left(\sum_{n=1}^{12}b_n\right)\cdot\sin\left(k\cdot\left(\omega t+\frac{\pi}{9}\right)\right)\right)\right]^2 dt} \\
ia_{2(rms)} = \sqrt{\frac{1}{T}\int_0^T \left[\frac{I_d\cdot\left(\frac{1}{1-Dboost}\right)}{2\pi^2}\sum_{k=1}^{\infty}\left(\left(\sum_{n=1}^{12}a_n\right)\cdot\cos\left(k\cdot\left(\omega t-\frac{\pi}{9}\right)\right)+\left(\sum_{n=1}^{12}b_n\right)\cdot\sin\left(k\cdot\left(\omega t-\frac{\pi}{9}\right)\right)\right)\right]^2 dt} \\
ib_{0(rms)} = \sqrt{\frac{1}{T}\int_0^T \left[\frac{I_d\cdot\left(\frac{1}{1-Dboost}\right)}{2\pi^2}\sum_{k=1}^{\infty}\left(\left(\sum_{n=1}^{12}a_n\right)\cdot\cos\left(k\cdot\left(\omega t+\frac{2\pi}{3}\right)\right)+\left(\sum_{n=1}^{12}b_n\right)\cdot\sin\left(k\cdot\left(\omega t+\frac{2\pi}{3}\right)\right)\right)\right]^2 dt} \\
ib_{1(rms)} = \sqrt{\frac{1}{T}\int_0^T \left[\frac{I_d\cdot\left(\frac{1}{1-Dboost}\right)}{2\pi^2}\sum_{k=1}^{\infty}\left(\left(\sum_{n=1}^{12}a_n\right)\cdot\cos\left(k\cdot\left(\omega t+\frac{7\pi}{9}\right)\right)+\left(\sum_{n=1}^{12}b_n\right)\cdot\sin\left(k\cdot\left(\omega t+\frac{7\pi}{9}\right)\right)\right)\right]^2 dt} \\
ib_{2(rms)} = \sqrt{\frac{1}{T}\int_0^T \left[\frac{I_d\cdot\left(\frac{1}{1-Dboost}\right)}{2\pi^2}\sum_{k=1}^{\infty}\left(\left(\sum_{n=1}^{12}a_n\right)\cdot\cos\left(k\cdot\left(\omega t+\frac{5\pi}{9}\right)\right)+\left(\sum_{n=1}^{12}b_n\right)\cdot\sin\left(k\cdot\left(\omega t+\frac{5\pi}{9}\right)\right)\right)\right]^2 dt} \\
ic_{0(rms)} = \sqrt{\frac{1}{T}\int_0^T \left[\frac{I_d\cdot\left(\frac{1}{1-Dboost}\right)}{2\pi^2}\sum_{k=1}^{\infty}\left(\left(\sum_{n=1}^{12}a_n\right)\cdot\cos\left(k\cdot\left(\omega t-\frac{2\pi}{3}\right)\right)+\left(\sum_{n=1}^{12}b_n\right)\cdot\sin\left(k\cdot\left(\omega t-\frac{2\pi}{3}\right)\right)\right)\right]^2 dt} \\
ic_{1(rms)} = \sqrt{\frac{1}{T}\int_0^T \left[\frac{I_d\cdot\left(\frac{1}{1-Dboost}\right)}{2\pi^2}\sum_{k=1}^{\infty}\left(\left(\sum_{n=1}^{12}a_n\right)\cdot\cos\left(k\cdot\left(\omega t-\frac{5\pi}{9}\right)\right)+\left(\sum_{n=1}^{12}b_n\right)\cdot\sin\left(k\cdot\left(\omega t-\frac{5\pi}{9}\right)\right)\right)\right]^2 dt} \\
ic_{2(rms)} = \sqrt{\frac{1}{T}\int_0^T \left[\frac{I_d\cdot\left(\frac{1}{1-Dboost}\right)}{2\pi^2}\sum_{k=1}^{\infty}\left(\left(\sum_{n=1}^{12}a_n\right)\cdot\cos\left(k\cdot\left(\omega t-\frac{7\pi}{9}\right)\right)+\left(\sum_{n=1}^{12}b_n\right)\cdot\sin\left(k\cdot\left(\omega t-\frac{7\pi}{9}\right)\right)\right)\right]^2 dt}
\end{cases} \tag{26}$$

$$\begin{cases}
ia_{(rms)} = \sqrt{\frac{1}{T}\int_0^T \left[\frac{2\sqrt{3}}{\pi}\cdot Id\cdot\left(\frac{1}{1-Dboost}\right)\cdot(\sin(\omega t))\right]^2 dt} \\
ib_{(rms)} = \sqrt{\frac{1}{T}\int_0^T \left[\frac{2\sqrt{3}}{\pi}\cdot Id\cdot\left(\frac{1}{1-Dboost}\right)\cdot\left(\sin\left(\omega t+\frac{2\pi}{3}\right)\right)\right]^2 dt} \\
ic_{(rms)} = \sqrt{\frac{1}{T}\int_0^T \left[\frac{2\sqrt{3}}{\pi}\cdot Id\cdot\left(\frac{1}{1-Dboost}\right)\cdot\left(\sin\left(\omega t-\frac{2\pi}{3}\right)\right)\right]^2 dt}
\end{cases} \tag{27}$$

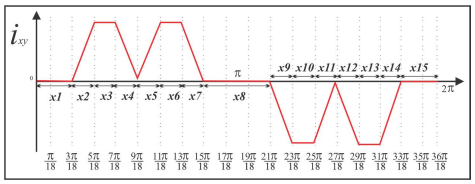

FIGURE 6. Detail of the current waveform imposed on the DDS-18PATRU.

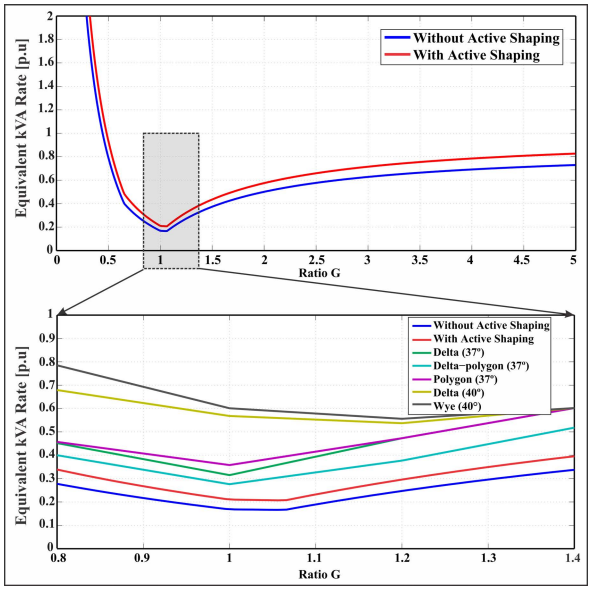

FIGURE 7. kVA rating of DDS18PATRU as a function of voltage gain: on the top - with and without active shaping technique; on the botton – detail of the behavior of the kVA rating compared to the results presented in [25].

A. CONTROL STRATEGY FOR ACTIVE CURRENT SHAPING

The block diagram of the developed control strategy is illustrated in Fig. 9. It was implemented through algorithms in C language, using the microcontroller TMS320F28379D with dual-core architecture. The output voltage control loop together with the algorithm for reference current waveform generation are managed by one core of the microcontroller with a sample rate frequency of 200kHz. The current controller operates in parallel using the second core of the microcontroller with Control Law Accelerator (CLA) at the same sample rate frequency. The synchronism between the input line currents and the supply voltage is assured using a Phase-Locked Loop (PLL) technique called SOGI-PLL [38].

TABLE 2. Specifications of the DDS-18PATRU.

Symbol	Parameter	Value
-	Input Voltage: Va, Vb, Vc	115/400Hz- Three-Phase
-	Primaries: N_{ab}, N_{bc} N_{ca}	28 AWG/241.3 coils
-	Auxiliaries 1 and 2: N_{ab1}, N_{ab2}, N_{bc1}, N_{bc2}, N_{ca1}, N_{ca2}	18 AWG/9.66 coils
-	Auxiliaries 3 and 4: N_{ab3}, N_{ab4}, N_{bc3}, N_{bc4}, N_{ca3}, N_{ca4}	18 AWG/42.616 coils
-	Core Material	Three-limb-stalloy
-	Core Type	Nippon BSD25/25/50
-	Stalloy Thickness	0.27 mm
Ae	Cross Section	8 cm^2
Aw	Window Area	10 cm^2
Bm	Maximum Magnetic Flux Density	1.4 T
J	Current Density	6 A/mm^2
We	Weight	3.93 kg
Ku	Window Utilization Factor	0.4
Kf	Window Coefficient	4.44
PCu	Copper losses	49.18 W
PFe	Iron losses	7.82 W
MLT	Mean Length Turn	22.44
-	Watts/kilogram	1.99

$$V_o = \frac{6}{2\pi}\int_{\frac{\pi}{3}}^{\frac{2\pi}{3}} \sqrt{6}\cdot v_x \cdot \sin(\omega t)d\omega t = \frac{3\cdot\sqrt{6}\cdot v_x}{\pi} = 2.339\cdot v_x \tag{31}$$

$$kVA_{rating}[\%] = \frac{S_{core}}{P_0} = \frac{\frac{1}{2}\cdot\left(3\cdot|v_{xx}|\cdot i_{xy} + 6\cdot\left|v_{xx1,2}\right|\cdot i_{x1,2} + 6\cdot\left|v_{xx3,4}\right|\cdot i_{x3,4} + 6\cdot|v_{xxn}|\cdot i_{xn}\right)}{2.339\cdot G\cdot v_x\cdot Id\cdot\left(\frac{1}{1-Dboost}\right)}\cdot 100 \tag{32}$$

$$kVA_{rating}[\%] = \frac{S_{core}}{P_0} = \frac{\frac{1}{2}\cdot\left(20.4\cdot Id\cdot\left(\frac{1}{1-Dboost}\right) + 6\cdot\left|V_{xx1,2}\right|\cdot 0.27\cdot Id\cdot\left(\frac{1}{1-Dboost}\right) + 6\cdot\left|V_{xx3,4}\right|\cdot 0.27\cdot Id\cdot\left(\frac{1}{1-Dboost}\right)\right)}{2.339\cdot v_x\cdot G\cdot Id\cdot\left(\frac{1}{1-Dboost}\right)}$$
$$\cdot 100 = 16.82\% \tag{33}$$

$$\begin{cases} ixy_{(rms)} = 0.305\cdot Id\cdot\left(\dfrac{1}{1-Dboost}\right) \\ ixx_{(rms)} = 0.057\cdot Id\cdot\left(\dfrac{1}{1-Dboost}\right) \end{cases} \tag{34}$$

$$kVA_{rating}[\%] = \frac{S_{core}}{P_0} = \frac{\frac{1}{2}\cdot\left(34.2\cdot Id\cdot\left(\frac{1}{1-Dboost}\right) + 6\cdot\left|V_{xx1,2}\right|\cdot 0.305\cdot Id\cdot\left(\frac{1}{1-Dboost}\right) + 6\cdot\left|V_{xx3,4}\right|\cdot 0.305\cdot Id\cdot\left(\frac{1}{1-Dboost}\right)\right)}{2.339\cdot v_x\cdot G\cdot Id\cdot\left(\frac{1}{1-Dboost}\right)}$$
$$\cdot 100 = 21.03\% \tag{35}$$

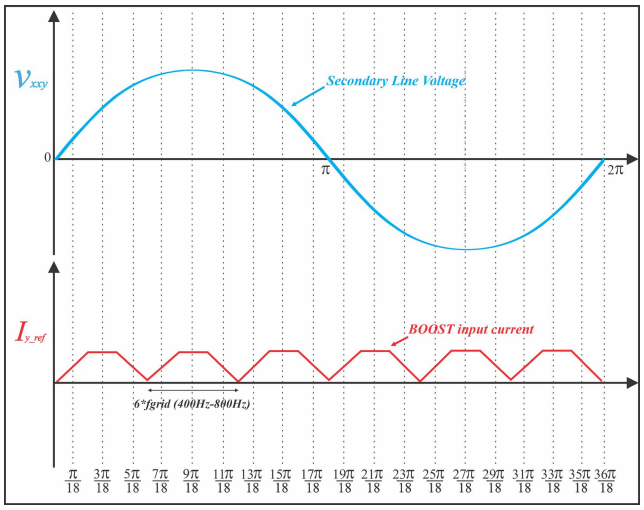

FIGURE 8. Details of the current waveform imposed on the input inductors of each Boost converter.

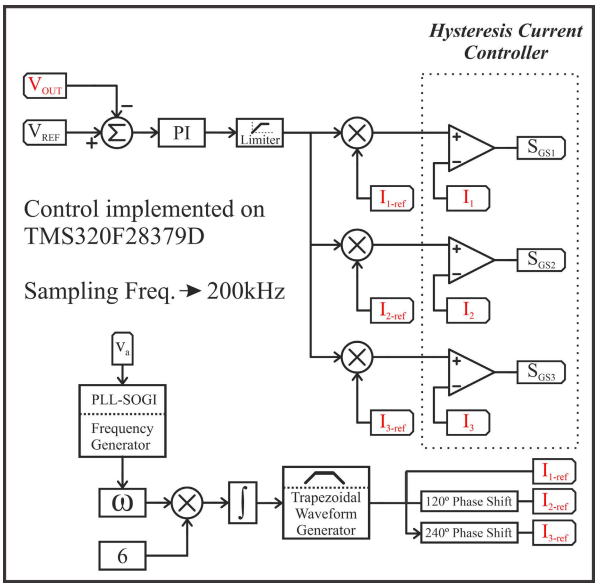

FIGURE 9. Simplified block diagram illustrating the developed control strategy.

TABLE 3. Specifications of Boost converters.

Parameter	Value
Power output for each converter	400 W
Maximum switching frequency	100kHz
Input inductances (L1, L2, …, L6)	1mH
Switches Q1, Q2 and Q3	SIC MOSFET C3M0120100K (22A/1000V)
Output Diodes (Dout1, Dout2, …, Dout6)	C3D10065A (10A / 650V)
Duty Cycle	0.478

In light of the aforementioned, one notes that the input for executing SOGI-PLL is the input voltage *Vab*. The angular frequency (ω) is obtained and multiplied by six, in order that its integration allows for the generating of the triangular waveform. This is the input for the algorithm dedicated to generating the desired trapezoidal waveform for the control of each Boost converter input current. It is important to emphasize that this procedure is better than the zero crossing detector (ZCD) method used in [32] and [33], as it avoids any delay of synchronism during transients. To conclude, the generated Boost current references signals ($I_{1\text{-ref}}$, $I_{2\text{-ref}}$, $I_{3\text{-ref}}$) are multiplied by the control voltage given by the output proportional-integral (PI) voltage controller.

To control the input current for each Boost converter, the Hysteresis controller was deployed due to its speed and excellent dynamic performance for a wide range of load variation [39]–[44]. In the current hysteresis loops, the same voltage compensator signal guarantees the balance between the currents with the aim of assuring the correct load power division and therefore, the correct composition of the grid currents. Thriugh the comparison of the feedback signal (I_1, I_2, I_3) with the current reference signal, one obtains the command signal for the switch of each Boost converter. The switching frequency is therefore variable, arriving at a maximum of 100 kHz.

B. AVERAGE STATE-SPACE MODEL FOR DETERMINING THE TRANSFER FUNCTIONS OF THE PLANT AND THE VOLTAGE CONTROLLER

The block diagram of the equivalent system of the proposed control strategy can be represented through Fig. 6, in which it is possible to design the voltage controller based on the analysis of the equivalent transfer function of the open loop system *Gvouti1,2,0(S)*, where the behavior of the output voltage for disturbances of the input current can be modeled by a first-order response. The additional blocks refer to hysteresis modulation and the reference current multiplier.

The transfer function from the Boost converter can be obtained through an analysis of average state space [37]. With the data presented in Table 2, the transfer function $G_{vouti1,2,0}(S)$ is given by (41).

$$G_{Vouti1,2,0} = \frac{R_{out} \cdot (1 - Dboost)}{C_{out} \cdot R_{out} \cdot s + 1} = \frac{348}{s + 2.74} \quad (41)$$

Therefore, the SISOTOOL from the software *MATLAB*® was used to obtain the output voltage compensator and to analyze the performance of the internal voltage loop control. From the *Tustin* method, the discrete transference function is given by (42) and directly after, the different compensator equations are given by (43) and (44). Finally, the equivalent transfer function of the voltage compensator is given by (45).

The Simulink tool from the software *MATLAB*® was used to simulate the complete system in closed loop, as represented in Fig. 11. One notes from the step response an overshot of around 5.79% and then it comes into steady state at about 111.0ms, which demonstrates that the voltage controller has

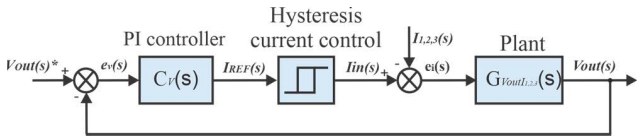

FIGURE 10. Block Diagram of the proposed control strategy.

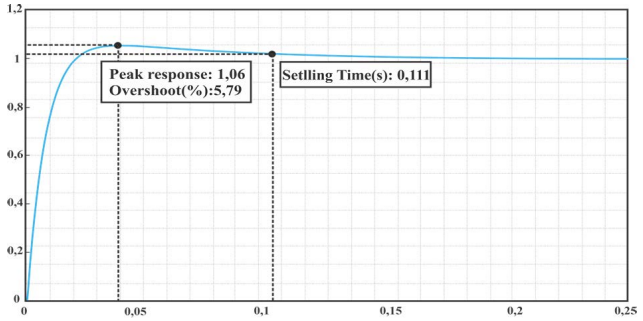

FIGURE 11. Step response of the system in closed loop.

a rapid enough response for the control of the output voltage, as desired. In Fig. 12 the respective *Root Locus* of the internal voltage loop is depicted, which proves the stability of the system. For the PI controller design specifications, the gain margin was set to crossover frequency is 22.1 Hz and phase margin of 85.1°.

$$\frac{K_v(s)}{E_v(s)} = \frac{0.402 \cdot (0.067 \cdot s + 1)}{0.067 \cdot s} \tag{42}$$

$$\frac{K_v(s)}{E_v(s)} = \frac{0.402015 - 0.401985 \cdot z^{-1}}{1 - z^{-1}} \tag{43}$$

$$\frac{K_v(s) \cdot z}{E_v(s) \cdot z} = \left(\frac{0.402015 \cdot z - 0.401985}{z - 1}\right) \tag{44}$$

Therefore, (44) can be represented by (45)

$$K_v[k] \cdot z = K_v[k-1] + 0.40215 \cdot E_v[k] - 0.401985 \cdot E_v[k-1] \tag{45}$$

where:

- Kv - Transference functions of the voltage compensators.
- Ev - Error signal between the reference and the signal captured by the sensors.
- k - Present sample.
- $k-$ 1 - Previous sample.

IV. EXPERIMENTAL RESULTS AND DISCUSSIONS

With the aim of validating the efficacy of the proposed solution, a prototype of 1.2 kW was developed and analyzed in the laboratory, as illustrated in Fig. 13. In Tables 1 and 2, the specifications of the implemented RU-DDS18PATR+Boost are presented.

In Fig. 14, the line-to-line voltages *vab0* corresponding to the secondary voltage are in phase with the mains supplies voltage *vab*. The rms values of *vab0* and *vab* are the same and

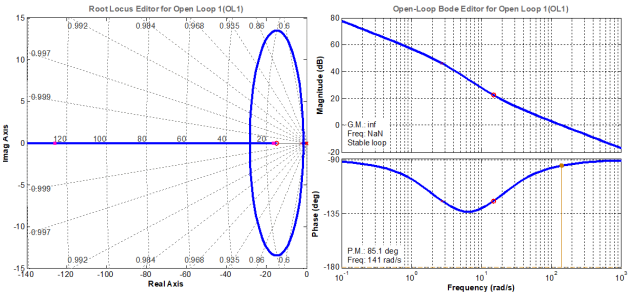

FIGURE 12. Root locus of the internal voltage loop.

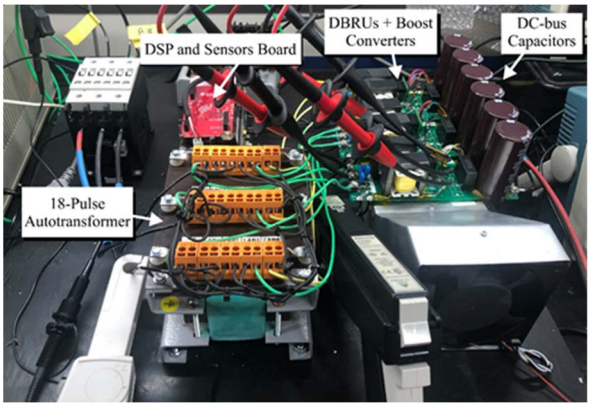

FIGURE 13. Picture of the 1.2kW RU-DDS18PATR+Boost prototype.

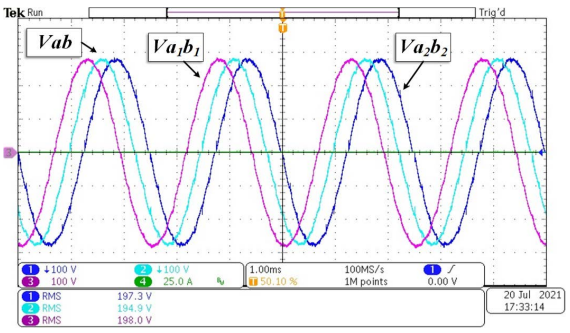

FIGURE 14. Picture of the 1.2kW RU-DDS18PATR+Boost prototype.

equal to 195.0 V. The voltage across the auxiliary windings gives the secondary line-to-line voltage, where *vab1* has a phase shift equal to +20°, and *vab2* has a phase shift equal to −20°, both regarding *vab0*.

Once that the correct operation of the DDS-18PATRU has been verified, two series of tests were carried out (operation modes shown in Fig. 4), the first was performed with the Boost converters operating with direct current imposed on the input inductors, and the second was performed with the imposition of trapezoidal waveform currents. With Boost converters operating with direct current imposed on the input inductors, the performance of the RU-DDS18PATR+Boost is similar to an 18-pulse ATRU. Here, the individual input line current harmonics of the 17th, 19th, 35th and 37th orders

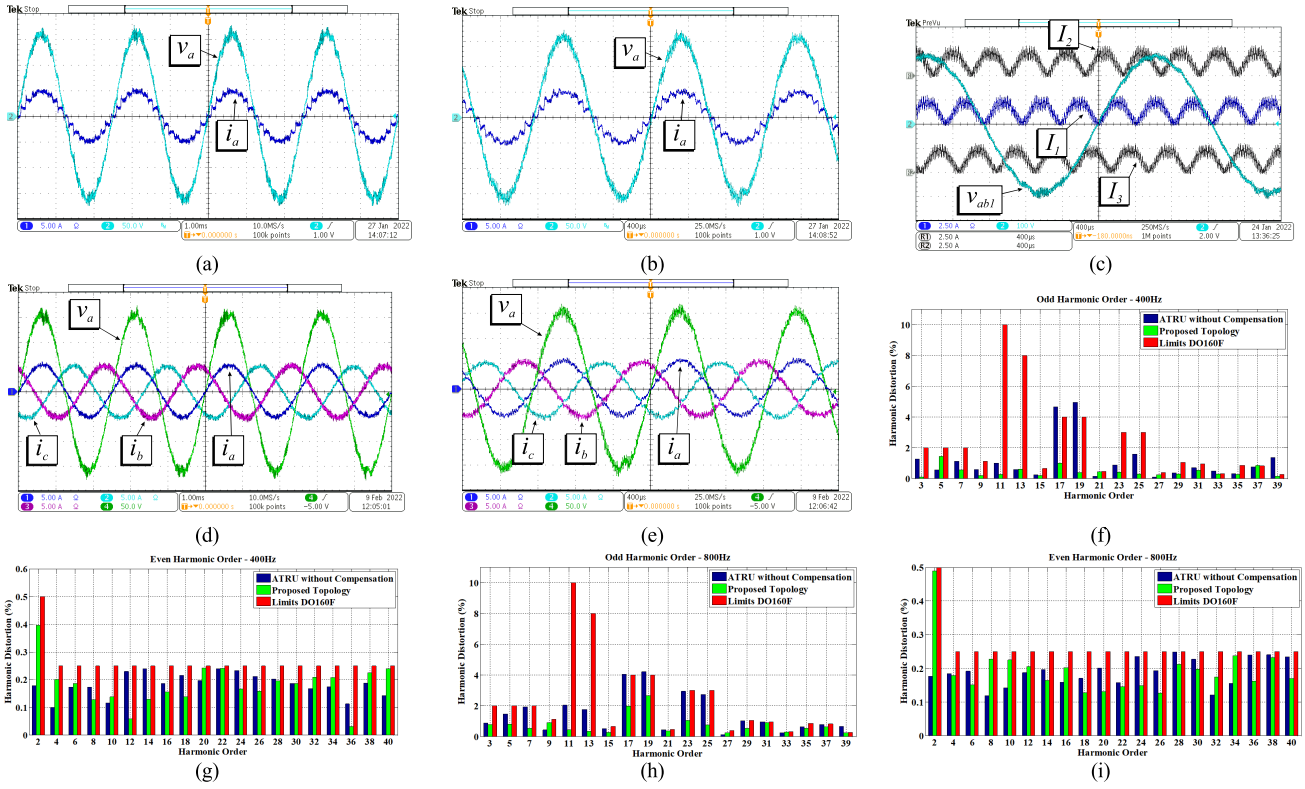

FIGURE 15. Power supply voltage and current without active current shaping at (a) 400Hz and (b) 800Hz; (c) current flowing through Boos input inductors with trapezoidal waveforms; Power supply voltage and current with active current shaping at (d) 400Hz and (e) 800Hz; Frequency spectrum of the input line current (f) odd harmonics at 400 Hz (g) even harmonics at 400 Hz (h) odd harmonics at 800 Hz (i) even harmonics at 800 Hz.

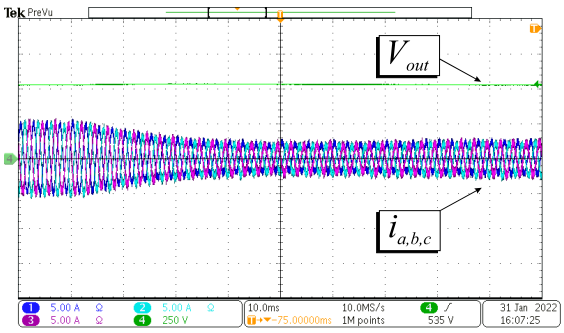

FIGURE 16. Load step from 100% to 50% of rated power at 400Hz (250 V/div, 5 A/div, and 10 ms/div).

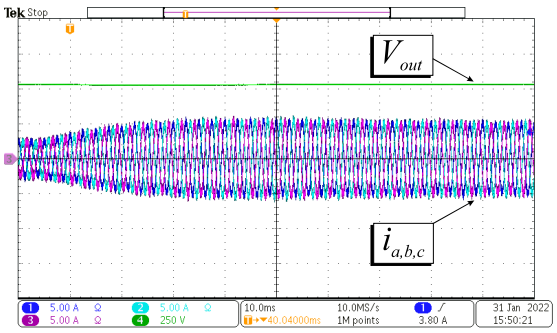

FIGURE 17. Load step from 50% to 100% of rated power at 400Hz (250 V/div, 5 A/div, and 10 ms/div).

exceed the harmonic content restrictions imposed by the DO-160F standard, as noted in Fig. 15.

By imposing a trapezoidal current on the input inductors of the Boost converters (active current shaping mode), as seen in Fig. 15(b), the current flowing between the DDS-18PATRU windings increases, for the same power processing required by the load, raising the kVA rating from 15.35% to 17%.

Through the analysis of Figs. 15(f)-15(i), one can observe that the harmonic content restrictions imposed by the DO-160F standard are met. Blue color is associated with the RU-DDS18PATR+Boost operating like an ordinary 18-pulse ATRU, the green color is associated with the RU-DDS18PATR+Boost operating with trapezoidal current shaping, and the red color indicates the harmonic content imposed by the DO-160F standard. The THDi of the input line currents was calculated using *MATLAB*®.

The final THDi achieved without active current shaping was 10.34% for 400Hz and 12.47% for 800Hz. With the imposition of a trapezoidal waveform on the current flowing through the inductor of each Boost converter, the final THDi achieved was 3.66% for 400Hz and 5.16% for 800Hz. In both cases the result achieved is lower than the limit imposed by DO-160F (15.26%).

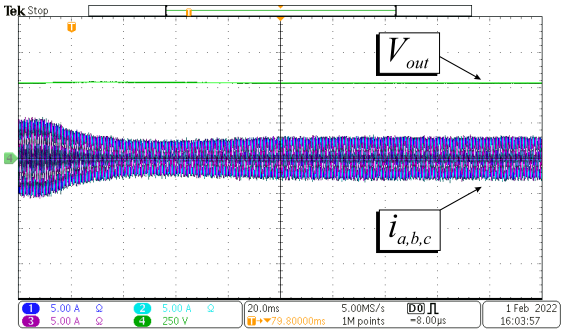

FIGURE 18. Load step from 100% to 50% of rated power at 800Hz (250 V/div, 5 A/div, and 10 ms/div).

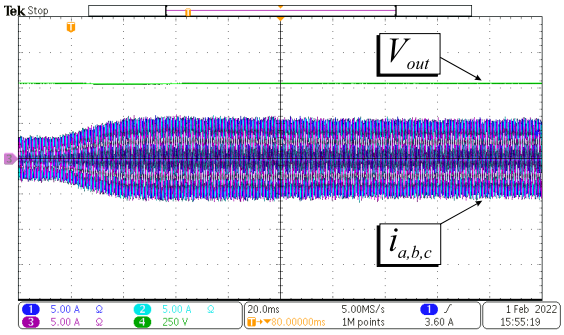

FIGURE 19. Load step from 50% to 100% of rated power at 800Hz (250 V/div, 5 A/div, and 10 ms/div).

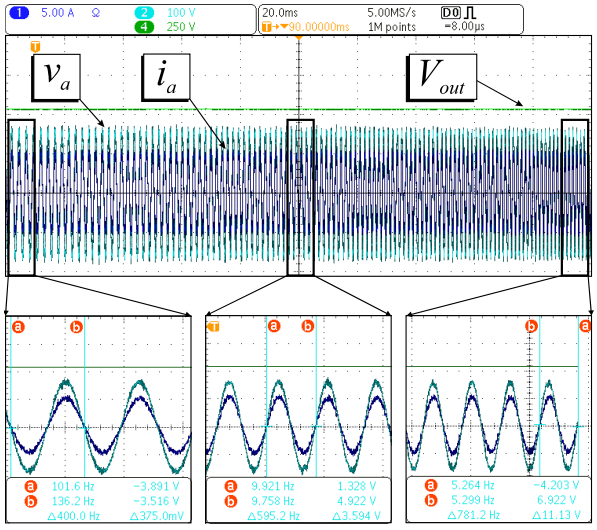

FIGURE 20. Syncronism between grid voltage and current during frequency variation (from the left to the right: 400Hz, 600Hz, and 800Hz - phase A for example).

The dynamic response of the output voltage controller and the Boost input current controller, when subjected to a 50% load step down and over, can be seen from Figs. 16 to 19, for both 400Hz and 800Hz operation.

Figure 20 shows the behavior of the structure facing variation of the grid power supply frequency, proving that the autotransformer can operate without having problems associated with core saturation. The perfect synchronism between current and voltage is also noted. Finally, in Fig. 21, the results concerning efficiency, THDi, and power factor for a wide load range are presented. The digital power meter Yokogawa WT230 was used to measure the output active power and the input apparent power. The results for the efficiency analysis show that 96% was achieved for rated load power. Noted here also is that the THDi decreases with increasing load power, so both the power factor and the efficiency increase.

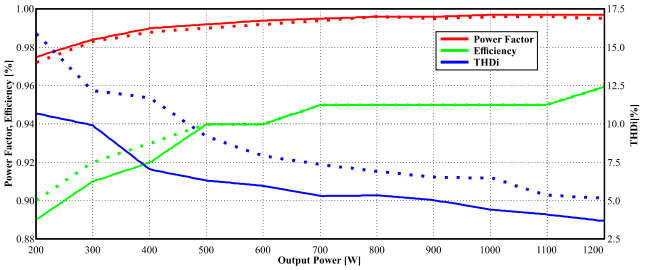

FIGURE 21. Analysis of THDi, Efficiency and Power Factor for wide load range (dashed line: 800Hz, continuous line: 400Hz).

V. CONCLUSION

In this study, an 18-pulse delta-differential rectifier was designed, analyzed, and proposed for MEA applications. An analytical comparison of the topology was performed in terms of power density, efficiency, and reliability, along with the relevant results being presented. Operating without active shaping or as an ordinary 18-ATRU, the obtained kVA rating of the ATRU is 16.82%. On the other hand, when operating with active current shaping, the peak value of the input inductor current of each Boost converter is increased. This elevation must be taken into account for the correct calculation of RMS currents. Therefore, in order to comply with individual harmonic content restrictions imposed by the DO-160F standard the new kVA rating is around 21.03%, which is still very small and can provide high power density and robustness, as well as reduced weight and volume for integrated DC distribution systems.

A prototype has been implemented and fully demonstrated in the laboratory, where it has been shown to operate with excellent performance, thus making it a good choice for MEA application.

The delta-differential autotransformer with a generalized connection, although presenting a higher number of secondary windings — when compared to other autotransformer topologies presented a more compact structure in terms of the other models analyzed, as it possesses a unitary transformation ratio.

Highlighted also is that the voltage level adjustment on the dc bus can be reached through the set-up of the cascaded dc-dc converters, with an 18-ATRU kVA rating of 21.03%. The level of efficiency reached was similar to the other studies analyzed — around 96% — leaving only to highlight the reduced number of semiconductors used, which stimulates a reduction in costs and increases reliability.

ACKNOWLEDGMENT

The authors extend their appreciation to Professors João Batista Vieira Júnior and Luiz Carlos de Freitas for funding this work under grants 304489/2017-4 and 304479/2017-9 provided by National Council for Scientific and Technological Development (CNPq).

REFERENCES

[1] L. Dorn-Gomba, J. Ramoul, J. Reimers, and A. Emadi, "Power electronic converters in electric aircraft: Current status, challenges, and emerging technologies," *IEEE Trans. Transport. Electrific.*, vol. 6, no. 4, pp. 1648–1664, Dec. 2020.

[2] B. Rahrovi and M. Ehsani, "A review of the more electric aircraft power electronics," in *Proc. IEEE Texas Power Energy Conf. (TPEC)*, Feb. 2019, pp. 1–6, doi: 10.1109/TPEC.2019.8662158.

[3] A. Barzkar and M. Ghassemi, "Electric power systems in more and all electric aircraft: A review," *IEEE Access*, vol. 8, pp. 169314–169332, 2020, doi: 10.1109/ACCESS.2020.3024168.

[4] *Aircraft Electric Power Characteristics*, Standard Military MIL-STD-704F, Department of Defense Standard, 2004.

[5] RTCA Inc. *Enviromental Conditions and Test Procedures for Airborne Equipment RTCA DO-160F*. RTCA Inc. [Online]. Available: http://www.rtca.org

[6] *Aerospace Characteristics of Aircraft Electrical Systems*, Standard ISO 1540, 2006. [Online]. Available: https://www.iso.org/standard/42067.html

[7] J. Chen, Y. Shen, J. Chen, H. Bai, C. Gong, and F. Wang, "Evaluation on the autoconfigured multipulse AC/DC rectifiers and their application in more electric aircrafts," *IEEE Trans. Transport. Electrific.*, vol. 6, no. 4, pp. 1721–1739, Dec. 2020, doi: 10.1109/TTE.2020.2983858.

[8] J. Brombach, A. Lücken, B. Nya, M. Johannsen, and D. Schulz, "Comparison of different electrical HVDC-architectures for aircraft application," in *Proc. Elect. Syst. Aircr., Railway Ship Propuls.*, Dec. 2012, pp. 1–6, doi: 10.1109/ESARS.2012.6387380.

[9] L. Setlak and R. Kowalik, "Mathematical model and simulation of selected components of the EPS of the aircraft, providing the operation of onboard electrical equipment and systems in accordance with MEA/AEA concept," in *Proc. Prog. Appl. Electr. Eng. (PAEE)*, Jun. 2017, pp. 1–6, doi: 10.1109/PAEE.2017.8009007.

[10] S. Zhao, M. Silva, J. A. Oliver, P. Alou, O. Garcia, and J. A. Cobos, "Analysis and design of an isolated single-stage three-phase full-bridge with current injection path PFC rectifier for aircraft application," in *Proc. IEEE Energy Convers. Congr. Expo. (ECCE)*, Sep. 2015, pp. 6777–6784, doi: 10.1109/ECCE.2015.7310608.

[11] G. Buticchi, C. Gerada, Y. J. Ko, and M. Liserre, "A smart transformer-rectifier unit for the more electric aircraft," in *Proc. IEEE 27th Int. Symp. Ind. Electron. (ISIE)*, Jun. 2018, pp. 324–328, doi: 10.1109/ISIE.2018.8433784.

[12] S. Gangavarapu and A. K. Rathore, "Three-phase interleaved semi-controlled PFC converter for aircraft application," in *Proc. IECON 43rd Annu. Conf. IEEE Ind. Electron. Soc.*, Oct. 2017, pp. 6652–6657, doi: 10.1109/IECON.2017.8217161.

[13] R. A. Mastromauro, S. Pugliese, and S. Stasi, "An advanced active rectifier based on the single-star bridge cells modular multilevel cascade converter for more-electric-aircrafts applications," in *Proc. Int. Conf. Electr. Syst. Aircr., Railway, Ship Propuls. Road Vehicles (ESARS)*, Mar. 2015, pp. 1–5, doi: 10.1109/ESARS.2015.7101421.

[14] Y. Zhao, W. Huang, and F. Bu, "DC voltage balancing strategy of a bipolar-output active rectifier for more electric aircraft based on zero vector redistribution," *IEEE Access*, vol. 9, pp. 139657–139667, 2021, doi: 10.1109/ACCESS.2021.3119058.

[15] S. Choi, "A three-phase unity-power-factor diode rectifier with active input current shaping," *IEEE Trans. Ind. Electron.*, vol. 52, no. 6, pp. 1711–1714, Dec. 2005, doi: 10.1109/TIE.2005.858699.

[16] S. Gangavarapu and A. K. Rathore, "Analysis and design of interleaved DCM buck–boost derived three-phase PFC converter for MEA," *IEEE Trans. Transport. Electrific.*, vol. 7, no. 3, pp. 1954–1963, Sep. 2021, doi: 10.1109/TTE.2021.3056114.

[17] S. Gangavarapu and A. K. Rathore, "A three-phase single-sensor-based cuk-derived PFC converter with reduced number of components for more electric aircraft," *IEEE Trans. Transport. Electrific.*, vol. 6, no. 4, pp. 1767–1779, Dec. 2020, doi: 10.1109/TTE.2020.2988154.

[18] G. Gong, M. L. Heldwein, U. Drofenik, J. Minibock, K. Mino, and J. W. Kolar, "Comparative evaluation of three-phase high-power-factor AC-DC converter concepts for application in future more electric aircraft," *IEEE Trans. Ind. Electron.*, vol. 52, no. 3, pp. 727–737, Jun. 2005, doi: 10.1109/TIE.2005.843957.

[19] S. Yang, J. Wang, and W. Yang, "A novel 24-pulse diode rectifier with an auxiliary single-phase full-wave rectifier at DC side," *IEEE Trans. Power Electron.*, vol. 32, no. 3, pp. 1885–1893, Mar. 2017, doi: 10.1109/TPEL.2016.2560200.

[20] J. Chen, H. Bai, J. Chen, and C. Gong, "A novel parallel configured 48-pulse autotransformer rectifier for aviation application," *IEEE Trans. Power Electron.*, vol. 37, no. 2, pp. 2125–2138, Feb. 2022, doi: 10.1109/TPEL.2021.3106322.

[21] R. Abdollahi, G. B. Gharehpetian, and M. Davari, "A novel more electric aircraft power system rectifier based on a low-rating autotransformer," *IEEE Trans. Transport. Electrific.*, vol. 8, no. 1, pp. 649–659, Mar. 2022, doi: 10.1109/TTE.2021.3104576.

[22] Saravana Prakash P, R. Kalpana, B. Singh, and G. Bhuvaneswari, "A 20-pulse asymmetric multiphase staggering autoconfigured transformer for power quality improvement," *IEEE Trans. Power Electron.*, vol. 33, no. 9, pp. 917–925, Feb. 2018, doi: 10.1109/TPEL.2017.2721958.

[23] R. Abdollahi and G. B. Gharehpetian, "A 20-pulse autotransformer rectifier unit for more electric aircrafts," *IEEE J. Emerg. Sel. Topics Power Electron.*, vol. 9, no. 3, pp. 2992–2999, Jun. 2021, doi: 10.1109/JESTPE.2020.2990670.

[24] T. Yang, S. Bozhko, and G. Asher, "Functional modeling of symmetrical multipulse autotransformer rectifier units for aerospace applications," *IEEE Trans. Power Electron.*, vol. 30, no. 9, pp. 4704–4713, Sep. 2015, doi: 10.1109/TPEL.2014.2364682.

[25] J. Chen, J. Shen, J. Chen, P. Shen, Q. Song, and C. Gong, "Investigation on the selection and design of step-up/down 18-pulse ATRUs for more electric aircrafts," *IEEE Trans. Transport. Electrific.*, vol. 5, no. 3, pp. 795–811, Sep. 2019, doi: 10.1109/TTE.2019.2930422.

[26] D. Yuan, S. Wang, and Y. Liu, "Dynamic phasor modeling of various multipulse rectifiers and a VSI fed by 18-pulse asymmetrical autotransformer rectifier unit for fast transient analysis," *IEEE Access*, vol. 8, pp. 43145–43155, 2020, doi: 10.1109/ACCESS.2020.2977270.

[27] A. Uan-Zo-li, R. P. Burgos, F. Lacaux, A. Roshan, F. Wang, and D. Boroyevich, "Analysis of new step-up and step-down direct symmetric 18-pulse topologies for aircraft autotransformer-rectifier units," in *Proc. IEEE 36th Power Electron. Spec. Conf.*, Jun. 2005, pp. 1142–1148, doi: 10.1109/PESC.2005.1581773.

[28] R. Burgos, A. Uan-Zo-Li, F. Lacaux, F. Wang, and D. Boroyevich, "Analysis and experimental evaluation of symmetric and asymmetric 18-pulse autotransformer rectifier topologies," in *Proc. Power Convers. Conf. Nagoya*, Apr. 2007, pp. 1286–1293, doi: 10.1109/PCCON.2007.373131.

[29] Y. Zhang, Z. Chen, B. Li, and Y. He, "Application of low harmonic 18-pulse rectifier power supply for radar power system," *IEEE Trans. Ind. Electron.*, vol. 66, no. 2, pp. 1080–1088, Feb. 2019, doi: 10.1109/TIE.2018.2831188.

[30] S. Khan, X. Zhang, M. Saad, H. Ali, B. M. Khan, and H. Zaman, "Comparative analysis of 18-pulse autotransformer rectifier unit topologies with intrinsic harmonic current cancellation," *Energies*, vol. 11, no. 6, p. 1347, 2018, doi: 10.3390/en11061347.

[31] T. Yang, S. Bozhko, P. Wheeler, S. Wang, and S. Wu, "Generic functional modelling of multi-pulse auto-transformer rectifier units for more-electric aircraft applications," *Chin. J. Aeronaut.*, vol. 31, no. 5, pp. 883–891, May 2018, doi: 10.1016/j.cja.2018.03.010.

[32] A. de Oliveira Costa Neto, A. L. Soares, G. B. de Lima, D. B. Rodrigues, E. A. A. Coelho, and L. C. G. Freitas, "Optimized 12-pulse rectifier with generalized delta connection autotransformer and isolated SEPIC converters for sinusoidal input line current imposition," *IEEE Trans. Power Electron.*, vol. 34, no. 4, pp. 3204–3213, Apr. 2019, doi: 10.1109/TPEL.2018.2850280.

[33] A. C. Lourenco, F. J. M. Seixas, J. C. Pelicer, and P. S. Oliveira, "18-pulse autotransformer rectifier unit using SEPIC converters for regulated DC-bus and high frequency isolation," in *Proc. IEEE 13th Brazilian Power Electron. Conf. 1st Southern Power Electron. Conf. (COBEP/SPEC)*, Nov. 2015, pp. 1–6, doi: 10.1109/COBEP.2015.7420041.

[34] P. Huang, C. Mao, D. Wang, L. Wang, Y. Duan, J. Qiu, G. Xu, and H. Cai, "Optimal design and implementation of high-voltage high-power silicon steel core medium-frequency transformer," *IEEE Trans. Ind. Electron.*, vol. 64, no. 6, pp. 4391–4401, Jun. 2017, doi: 10.1109/TIE.2017.2674591.

[35] C. W. T. McLyman, "Three-phase transformer design," in *Transformer and Inductor Design Handbook*, 4th ed. Oxfordshire, U.K.: Taylor & Francis Group, LCC, 2011.
[36] *Power Transformers—Part 11–Dry Type Transformers*, document IEC 60076-11, 2004.
[37] R. W. Erickson and D. Maksimovic, "Principles of steady-state converter analysis," in *Fundamental of Power Electronics*, 3rd ed. Denver, CO, USA, Springer, 2020.
[38] R. Teodorescu, M. Liserre, and P. Rodrigues, "Grid synchronization in single-phase power converters," in *Grid Converters for Photovoltaic Wind Power Systems*. New York, NY, USA: Wiley, 2011.
[39] A. V. Costa, "New hybrid high-power rectifier with reduced THDI and voltage-sag ride-through capability using boost converter," *IEEE Trans. Ind. Appl.*, vol. 49, no. 6, pp. 2421–2436, Nov. 2013, doi: 10.1109/TIA.2013.2262914.
[40] D. B. Rodrigues, A. V. Costa, G. B. Lima, L. C. de Freitas, E. A. A. Coelho, V. J. Farias, and L. C. G. Freitas, "DSP-based implementation of control strategy for sinusoidal input line current imposition for a hybrid three-phase rectifier," *IEEE Trans. Ind. Informat.*, vol. 9, no. 4, pp. 1947–1963, Nov. 2013, doi: 10.1109/TII.2012.2227268.
[41] L. H. S. C. Barreto, E. A. A. Coelho, V. J. Farias, L. C. D. Freitas, and J. J. B. Vieira, "The bang-bang hysteresis current waveshaping control technique used to implement a high power factor power supply," *IEEE Trans. Power Electron.*, vol. 19, no. 1, pp. 160–168, Jan. 2004, doi: 10.1109/TPEL.2003.820591.
[42] I. Rasoanarivo, K. Arab-Tehrani, and F.-M. Sargos, "Fractional order PID and modulated hysteresis for high performance current control in multi-level inverters," in *Proc. IEEE Ind. Appl. Soc. Annu. Meeting*, Oct. 2011, pp. 1–7, doi: 10.1109/IAS.2011.6074351.
[43] I. Rasoanarivo, S. Brechet, A. Battiston, and B. Nahid-Mobarakeh, "Behavioral analysis of a boost converter with high performance source filter and a fractional-order PID controller," in *Proc. IEEE Ind. Appl. Soc. Annu. Meeting*, Oct. 2012, pp. 1–6.
[44] W. Stefanutti and P. Mattavelli, "Fully digital hysteresis modulation with switching-time prediction," *IEEE Trans. Ind. Appl.*, vol. 42, no. 3, pp. 763–769, May 2006, doi: 10.1109/TIA.2006.873665.

ANA L. SOARES was born in Bom Despacho, Minas Gerais, Brazil. She received the B.Sc. and M.Sc. degrees in electrical engineering from the Federal University of Uberlândia (UFU), Minas Gerais, in 2017 and 2019, respectively. She is currently pursuing the Ph.D. degree. Her research interests include power electronics, power factor correction, multipulse transformer applications, and more electric aircraft (MEA).

ANTÔNIO C. O. NETO was born in Uberlândia, Brazil, in 1992. He received the B.Sc. and M.Sc. degrees in electrical engineering from the Universidade Federal de Uberlândia, Uberlândia, in 2015 and 2018, respectively. He is currently pursuing the Ph.D. degree in the research nucleus in power electronics with the Faculty of Electrical Engineering. His research interests include multipulse converters, digital control applied to power electronics, and power factor correction.

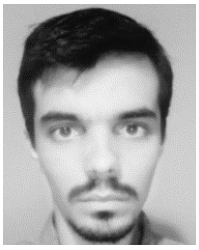

VITOR F. BARBOSA received the B.Sc. degree from the Federal University of Triângulo Mineiro (UFTM), in 2017, and the M.Sc. degree from the Federal University of Uberlândia (UFU), in 2020. He is currently pursuing the Ph.D. degree in electrical engineering. His research interests include active power factor correction, digital signal processing, switched converters, hybrid rectifiers, DC microgrids, and more electric aircraft (MEA).

GUSTAVO B. LIMA was born in Ibiassucê, Brazil, in 1986. He received the B.Sc., M.Sc., and Ph.D. degrees in electrical engineering from the Universidade Federal de Uberlândia, Uberlândia, Minas Gerais, Brazil, in 2010, 2012, and 2015, respectively. Since 2017, he has been with the Federal University of Uberlândia, where he has been developing teaching and research activities in the area of power electronics and power systems as a Professor Member of the Research Center in Power Electronics (NUPEP). His research interests include hybrid rectifiers, digital control applied to power electronics, and power factor correction.

LUIZ C. G. FREITAS was born in Uberlândia, Brazil, in 1976. He graduated in electrical engineering with emphasis on power systems from the Federal University of Uberlândia, in 2001, and the master's and Ph.D. degrees in electrical engineering with emphasis on power electronics from the Federal University of Uberlândia, in 2003 and 2006, respectively. In his doctoral thesis, he developed an innovative topological design of a three-phase hybrid rectifier for high power drive systems. In 2008, he joined the Faculty of the Federal University of Uberlândia, where he has been working developing teaching and research activities in the area of power electronics and power systems. Since 2010, he has been the Coordinator of the Research Center in Power Electronics (NUPEP) at UFU. Since 2013, he has been a Researcher recognized by the National Council for Scientific and Technological Development (CNPq) with a Research Productivity Grant. He has experience in the area of electrical engineering, with an emphasis on conversion and rectification of electric energy, working on various topics related to power electronics, electric power quality, and renewable energy. In 2012, he has received the Second Prize Paper Award of the IEEE-IAS-Industrial Automation and Control Committee (IACC) for his contribution to the development of hybrid rectifier structures.